OPEN BIOLOGY

royalsocietypublishing.org/journal/rsob

Research

Cite this article: Bamford RA *et al*. 2024 CNTN4 modulates neural elongation through interplay with APP. *Open Biol.* **14**: 240018.
https://doi.org/10.1098/rsob.240018

Received: 23 January 2024
Accepted: 4 March 2024

Subject Areas:
neuroscience, developmental biology, cellular biology

Keywords:
CNTN4, APP, cell, cortex, neuronal, motor

Author for correspondence:
Asami Oguro-Ando
e-mail: a.oguro-ando@exeter.ac.uk

Electronic supplementary material is available online at https://doi.org/10.6084/m9.figshare.c.7125279.

THE ROYAL SOCIETY PUBLISHING

CNTN4 modulates neural elongation through interplay with APP

Rosemary A. Bamford[1], Amila Zuko[2], Madeline Eve[1], Jan J. Sprengers[3], Harm Post[4,5], Renske L. R. E. Taggenbrock[3], Dominique Fäßler[6], Annika Mehr[6], Owen J. R. Jones[1], Aurimas Kudzinskas[1], Josan Gandawijaya[1], Ulrike C. Müller[6], Martien J. H. Kas[3,7], J. Peter H. Burbach[3] and Asami Oguro-Ando[1,8,9]

[1]University of Exeter Medical School, University of Exeter, Exeter EX2 5DW, UK
[2]Department of Molecular Neurobiology, Donders Institute for Brain, Cognition and Behaviour and Faculty of Science, Radboud University, Nijmegen, The Netherlands
[3]Department of Translational Neuroscience, UMC Utrecht Brain Center, UMC Utrecht, Utrecht 3508 AB, The Netherlands
[4]Biomolecular Mass Spectrometry and Proteomics, Bijvoet Center for Biomolecular Research and Utrecht, Institute for Pharmaceutical Sciences, Utrecht University, Utrecht, The Netherlands
[5]Netherlands Proteomics Centre, Utrecht, The Netherlands
[6]Institute for Pharmacy and Molecular Biotechnology (IPMB), Functional Genomics, University of Heidelberg, Heidelberg 69120, Germany
[7]Groningen Institute for Evolutionary Life Sciences, University of Groningen, Groningen, The Netherlands
[8]Department of Pharmacy, Faculty of Pharmaceutical Sciences, Tokyo University of Science, Noda, Chiba, Japan
[9]Research Institute for Science and Technology, Tokyo University of Science, Tokyo, Japan

JPHB, 0000-0002-8619-6168; AO-A, 0000-0003-4029-3250

The neuronal cell adhesion molecule contactin-4 (*CNTN4*) is genetically associated with autism spectrum disorder (ASD) and other psychiatric disorders. *Cntn4*-deficient mouse models have previously shown that CNTN4 plays important roles in axon guidance and synaptic plasticity in the hippocampus. However, the pathogenesis and functional role of CNTN4 in the cortex has not yet been investigated. Our study found a reduction in cortical thickness in the motor cortex of *Cntn4*$^{-/-}$ mice, but cortical cell migration and differentiation were unaffected. Significant morphological changes were observed in neurons in the M1 region of the motor cortex, indicating that CNTN4 is also involved in the morphology and spine density of neurons in the motor cortex. Furthermore, mass spectrometry analysis identified an interaction partner for CNTN4, confirming an interaction between CNTN4 and amyloid-precursor protein (APP). Knockout human cells for CNTN4 and/or APP revealed a relationship between CNTN4 and APP. This study demonstrates that CNTN4 contributes to cortical development and that binding and interplay with APP controls neural elongation. This is an important finding for understanding the physiological function of APP, a key protein for Alzheimer's disease. The binding between CNTN4 and APP, which is involved in neurodevelopment, is essential for healthy nerve outgrowth.

1. Introduction

Neurodevelopmental disorders such as autism spectrum disorder (ASD) are highly heterogeneous in terms of genetics, behaviour and pathology [1–3]. ASD is characterized by core behavioural domains such as impaired social communication and interactions, repetitive behaviour and restricted interests [1,2]. A clinical diagnosis of ASD is based primarily upon behaviour; however, ASD encompasses a range of syndromes and severity [3]. According to the Simons Foundation Autism Research Initiative, over 1000

genes have been implicated in ASD, and this list continues to grow [4]. However, the mechanisms of how current ASD-associated genes [4] influence neurodevelopment and are involved in ASD are not fully understood. It has been proposed that there are four converging molecular processes important to these genes: neuronal communication [5], neuronal cell adhesion [6], excitation and inhibition balance [7,8] and regulation of post-synaptic translation [9]. Neuronal cell adhesion gene networks, in particular those that are acting in the synaptic complex [10,11], are evidenced to be involved in ASD pathogenesis, and well-studied genes include neurexin-1 (*NRXN1*) [12], neuroligin-1 (*NLGN1*) [13,14], neuroligin-4 (*NLGN4*) [15] and contactin associated protein-2 (*CNTNAP2*) [16–19]. Cell adhesion molecules are integral to neuronal migration, axon guidance and neuron–glial cell interactions; processes important for cortical development and often disturbed in ASD [20–22]. ASD has been associated with abnormalities in the cerebral cortex and subsequently affected cognitive functions (i.e. communication, interaction and learning) [23] and multiple pathologies in cortical areas [24–26].

Contactins are a protein family belonging to a specific subclass of the immunoglobulin cell adhesion molecule superfamily (IgCAM). These proteins share 40–60% homology at the amino acid sequence level [27]. Contactins have been previously associated with neurodevelopmental disorders and constitute an interesting group of proteins to investigate in relation to ASD aetiology [28–30]. Copy number variants have been identified in cell adhesion molecules in ASD patients, which further suggests a role for this group of proteins in ASD development [31–34]. Among them, Contactin 4 (*CNTN4*) and Contactin 6 (*CNTN6*) have been reported as candidate genes for chromosome 3 disorders [6]. In particular, *CNTN4* has been previously linked to genetic, behaviour and pathological studies of ASD [35–38].

CNTN4 is mainly expressed in the cerebral cortex layers II–V in addition to the olfactory bulb, thalamus and hippocampus [38] as well as expressed on cortical pyramidal and interneurons [39]. The domains of human CNTN4 are conserved in mice [40], therefore, mouse models can be used to reveal the role of CNTN4 in normal and abnormal development. Kaneko-Goto *et al*. generated *Cntn4*-deficient mice and observed the importance of CNTN4 as an axon guidance molecule in the olfactory bulb [41], with further evidence in the optic system [42]. Therefore, CNTN4 acts as one of the axon guidance molecules crucial for the proper formation and development of the olfactory and optic systems [41,42]. More recently, Molenhuis *et al.* used a developmental behaviour battery to study *Cntn4*-deficient mice, which revealed subtle non-disease-specific changes in sensory behavioural responses and cognitive abilities [43], while Oguro-Ando *et al.* showed that *Cntn4* is associated with morphological and synaptic plasticity changes in hippocampal CA1 neurons and has important functions in fear memory in experiments using *Cntn4*-deficient mice [44]. However, since CNTN4 lacks transmembrane and intracellular domains, it is closely dependent on *cis* or *trans* interactions with membrane-spanning proteins [27]. Osterfield *et al.* [53] have previously shown a direct binding between CNTN4 and transmembrane amyloid-precursor protein (APP). Expression of APP in mice has been observed early in development and is ubiquitously expressed in adult mice [45–47]. The full extent of the molecular network with which CNTN4 interacts, as well as the role of CNTN4 in cortical and neuronal development, is still not clear.

The aim of this study was to identify novel functions of CNTN4 in the cortex at protein, cellular and anatomical levels using $Cntn4^{-/-}$ mice. This provides information on the role CNTN4 has in neurodevelopmental processes. We investigated the phenotype in the cortex of the $Cntn4^{-/-}$ mice and found that the disruption of neuroanatomical organization, caused as a consequence of *CNTN4* deficiency, was associated with structural and morphological changes in the cortex. We then examined the binding partners of CNTN4 and the impact of their interactions on the expression levels and morphology of human cell lines. Together, our data suggest that CNTN4 plays an important role in the motor cortex, which may lead to further insights into the aetiology of ASD and neurodevelopmental mechanisms.

2. Results

2.1. Abnormal cortical thickness observed in $Cntn4^{-/-}$ mice

In the cerebral cortex, the cortical layer thickness is related to neuroblast migration and may be an indicator of neurodevelopment abnormalities. Nissl staining and microscopic imaging of brain sections were carried out in order to measure the cortical layer thickness of $Cntn4^{-/-}$, $Cntn4^{+/-}$ and $Cntn4^{+/+}$ mice, respectively (figure 1*a*). The thickness of the upper layers (I–IV), lower layers (V–VI) and the total thickness were measured for the motor cortex, somatosensory cortex and visual cortex. Quantitative results showed that the cortical thickness of all layers for the somatosensory and visual cortices did not differ between the genotypes (electronic supplementary material, figure S1, $p > 0.05$, one-way ANOVA). However, the thickness of the upper layer of the motor cortex was significantly reduced in the $Cntn4^{-/-}$ mice (figure 1*b*, $p = 0.0188$, one-way ANOVA). Therefore, *Cntn4* deficiency leads to cortical thinning of the primary motor cortex, indicating abnormal gross cortical development.

2.2. Tissue architecture and cell differentiation influenced by loss of *Cntn4*

Next, we focused on the laminar positioning and numbers of specific cortical pyramidal neurons in the motor cortex of $Cntn4^{+/+}$, $Cntn4^{+/-}$ and $Cntn4^{-/-}$ mice. The location and density of upper- and lower-layer pyramidal neurons were investigated by visualization of neurons destined for layers II–IV (red, figure 1c) in adult mice using Cux1 as a marker. Cell counting revealed a significant decrease in the total number of neurons, which are NeuN+ (green, figure 1*c*, $p = 0.0058$, one-way ANOVA) in the upper layers (layers II–IV), between $Cntn4^{+/-}$ and $Cntn4^{-/-}$ mice (figure 1d). However, there was no significant difference in the total number of cells, which are DAPI+ (blue, figure 1*c*, $p > 0.05$, one-way ANOVA) in the upper layers between genotypes. There was a significant increase in Cux1/NeuN+ neurons in the upper layers for $Cntn4^{+/+}$ and $Cntn4^{-/-}$ mice with respect to

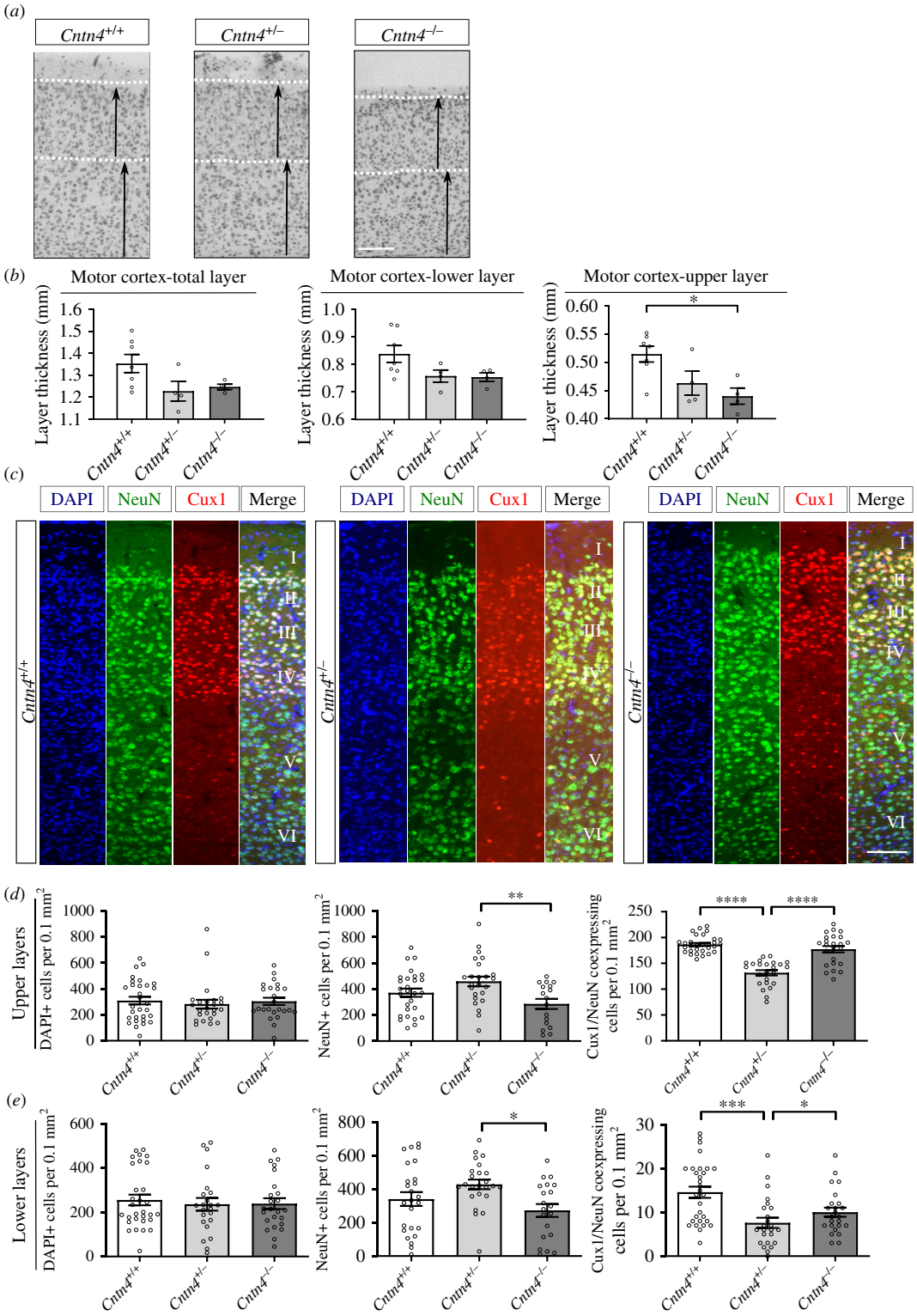

Figure 1. Cortical thickness and upper layer pyramidal neurons in *Cntn4*$^{-/-}$ mice. (*a*) Nissl-stained sections of the motor cortex of adult *Cntn4*$^{+/+}$, *Cntn4*$^{+/-}$ and *Cntn4*$^{-/-}$ mice. Arrows indicate upper and lower layer thickness. The scale bar indicates 250 µm. (*b*) Quantitative analysis of the represented cortical layer thickness (upper I–IV, lower V–VI and total) demonstrate a significant difference in motor cortex thickness in all layers between *Cntn4*$^{+/+}$ and *Cntn4*$^{-/-}$ mice. Analysis was performed, in each area, on at least three slices. Data are presented as mean ± s.e.m., *Cntn4*$^{+/+}$ ($n = 7$), *Cntn4*$^{+/-}$ ($n = 4$) and *Cntn4*$^{-/-}$ mice ($n = 4$), $p = 0.0188$ (upper layer, *Cntn4*$^{+/+}$ versus *Cntn4*$^{-/-}$). (*c*) Images of Cux1 expression (red) in layers II–IV of the motor cortex together with the NeuN (green) in adult *Cntn4*$^{+/+}$, *Cntn4*$^{+/-}$ and *Cntn4*$^{-/-}$ mice. DAPI is in blue. The scale bar represents 50 µm. (*d*) Quantitative analysis of the upper layers (layers II–IV) did not show differences in total cell number ($p > 0.05$, one-way ANOVA), but did show significant differences in total neuron number and Cux1+ neurons in the *Cntn4*$^{+/-}$ mice ($p = 0.0058$ and $p < 0.0001$, respectively, one-way ANOVA). (*e*) Quantitative analysis of the lower layers (layers V–VI) did not show differences in total cell number ($p > 0.05$, one-way ANOVA), but did show significant differences in total neuron number ($p = 0.013$, one-way ANOVA) and Cux1+ neurons ($p = 0.0201$, *Cntn4*$^{+/+}$ versus *Cntn4*$^{-/-}$; $p = 0.0002$, *Cntn4*$^{+/+}$ versus *Cntn4*$^{+/-}$, one-way ANOVA) in the *Cntn4*$^{+/-}$ mice. Analysis was performed, in each area, on at least six slices in *Cntn4*$^{+/+}$ ($n = 5$), *Cntn4*$^{+/-}$ ($n = 4$) and *Cntn4*$^{-/-}$ mice ($n = 4$) using unpaired Student's *t* test. Data are presented as mean ± s.e.m.

Cntn4$^{+/-}$ mice (figure 1*d*, $p < 0.0001$, one-way ANOVA). Measurements revealed no statistical difference in the total number of cells or of neurons (figure 1*e*, $p > 0.05$, one-way ANOVA). There was a significant decrease in the number of Cux1+ displaced

neurons in the lower layers (layers V–VI) of *Cntn4*$^{-/-}$ mice (figure 1*e*, $p = 0.0201$, *Cntn4*$^{+/+}$ versus *Cntn4*$^{-/-}$; $p = 0.0002$, *Cntn4*$^{+/+}$ versus *Cntn4*$^{+/-}$, one-way ANOVA). Similar to the upper layers, a significant decrease was observed in the total number of neurons which are NeuN+ (green, figure 1*c*) in the lower layers, between *Cntn4*$^{+/-}$ and *Cntn4*$^{-/-}$ mice (figure 1e , $p = 0.013$, one-way ANOVA). Overall, neuronal proportion and cortical migration differed in the M1 region but do not account for the cortical thinning observed in the Nissl staining. These results indicate that Cntn4 is required for normal development of pyramidal neurons in the upper layers of the motor cortex.

2.3. *Cntn4* deficiency affects dendrite length and complexity

In parallel to investigating the density and migration of Cntn4-deficient cortical pyramidal neurons, the morphology of Golgi-stained pyramidal neurons in the motor cortex layers II–III was analysed for dendrite length, branching and complexity in the *Cntn4*$^{+/+}$, *Cntn4*$^{+/-}$ and *Cntn4*$^{-/-}$ mice (figure 2*a,b*). The longest dendrite length was significantly decreased in the apical dendrites of the *Cntn4*$^{-/-}$ mice compared with the *Cntn4*$^{+/-}$ mice ($p = 0.0245$, one-way ANOVA) (figure 2*c*).

The dendritic complexity index (DCI) was calculated in order to compare the complexity of the branching dendrites and the length between pyramidal neurons. The more complex the branching structure, or longer the dendrites, the higher the index is. For the apical and basal dendrites, an equal complexity was observed across all genotypes (figure 2*c,e*, $p > 0.05$, one-way ANOVA). The number of apical and basal dendrite tips, and total intersections, was not significantly different between genotypes (figure 2*c,e*, $p > 0.05$, one-way ANOVA).

Sholl plots indicate the distribution of dendritic intersections and length at increasing distance from the centre of the cell body [48]. The last Sholl apical and basal intersections were not significantly different between genotypes (figure 2*c,e*, $p > 0.05$, one-way ANOVA). It was observed that the *Cntn4*$^{-/-}$ mice had a significantly higher number of Sholl apical intersections in the range of 50 µm from the soma compared with *Cntn4*$^{+/+}$ mice. The *Cntn4*$^{-/-}$ mice had significantly longer Sholl apical lengths in the range of 80 µm from the soma compared with the *Cntn4*$^{+/+}$ mice (figure 2*d*, $p < 0.05$, one-way ANOVA). It was observed that the *Cntn4*$^{-/-}$ mice had a significantly higher number of Sholl basal intersections within 20 µm from the soma compared with *Cntn4*$^{+/+}$ mice. The *Cntn4*$^{-/-}$ mice had significantly longer Sholl basal lengths within 30 µm from the soma compared with the *Cntn4*$^{+/+}$ mice (figure 2*f*, $p < 0.05$, one-way ANOVA). These data indicate that *Cntn4* deficiency causes abnormal apical and basal neurite growth in cortical pyramidal neurons.

2.4. Spine number and maturity are changed in *Cntn4*$^{-/-}$ mice

To further investigate the role of *Cntn4* in the cell function and fate of pyramidal neurons in the motor cortex, we employed Golgi staining to assess spine numbers and their maturity status (figure 3*a,b*). Loss of *Cntn4* significantly increased the total number of spines 50 µm from the cell soma compared with *Cntn4*$^{+/+}$ mice ($p = 0.0057$) (figure 3*c*). The maturity of spines also differed for the *Cntn4*-deficient mice; there were significantly fewer immature spines (A type) and more abnormal spines (F/G types) (figure 3*d,f*). These differences were more pronounced in the first 25 µm than in the latter 25 µm. Expression of the other spine morphologies was comparable between the genotypes. Since the total number of spines increases overall, this implies that loss of *Cntn4* expression leads to an increase of abnormal spines at the expense of immature spines which decrease in number.

2.5. *Cntn4* overexpression leads to longer neurites in primary culture

Primary cell culturing was conducted to evaluate the consequences of *Cntn4* overexpression (OE) on neurite outgrowth and cell body volume. Transfection of cortical neurons showed a significantly increased longest length of the dendrites ($p = 0.0415$, unpaired Student's *t* test), although the total length was not significantly different between empty vector (EV) and *Cntn4* OE neurons ($p > 0.05$, unpaired Student's *t* test) (figure 4*a,b*). No other morphological changes were observed in the neurons. No significant change in apoptosis was observed for *Cntn4* OE ($p > 0.05$, unpaired Student's *t* test) (figure 4*c*).

2.6. Identification of APP as interacting partner of Cntn4

In order to find proteins that interact with Cntn4 to exert its role, an unbiased proteomics approach using Cntn4 protein fused to the Plexin A2 transmembrane domain and GFP (Cntn4-TMGFPBio and control TMGFPBio) was used to identify binding partners of this protein after expression in HEK293 cells (figure 5*a,b*). These cells are known to express a large range of proteins [49] and have successfully been used before to find partners of other contactins [50]. Following immunoprecipitation (IP) experiments, Cntn4 fusions and control proteins were detected at 148 and 40 kDa, respectively, by Western blotting and Coomassie blue staining (figure 5*c,d*). Raw mass spectrometry data were analysed with the Mascot search engine and scores were assigned to identify peptides. In comparison with control experiments, confidence scores using Saint scoring [51] were assigned to the identified proteins. A ranked list of putative interacting proteins was obtained representing proteins that were significantly higher or exclusively present in the Cntn4 fusion protein pull-down samples (table 1). The highest scoring transmembrane proteins were the proteins radixin (RDX), amyloid-beta precursor protein (APP) and brain acid soluble protein 1 (BASP1).

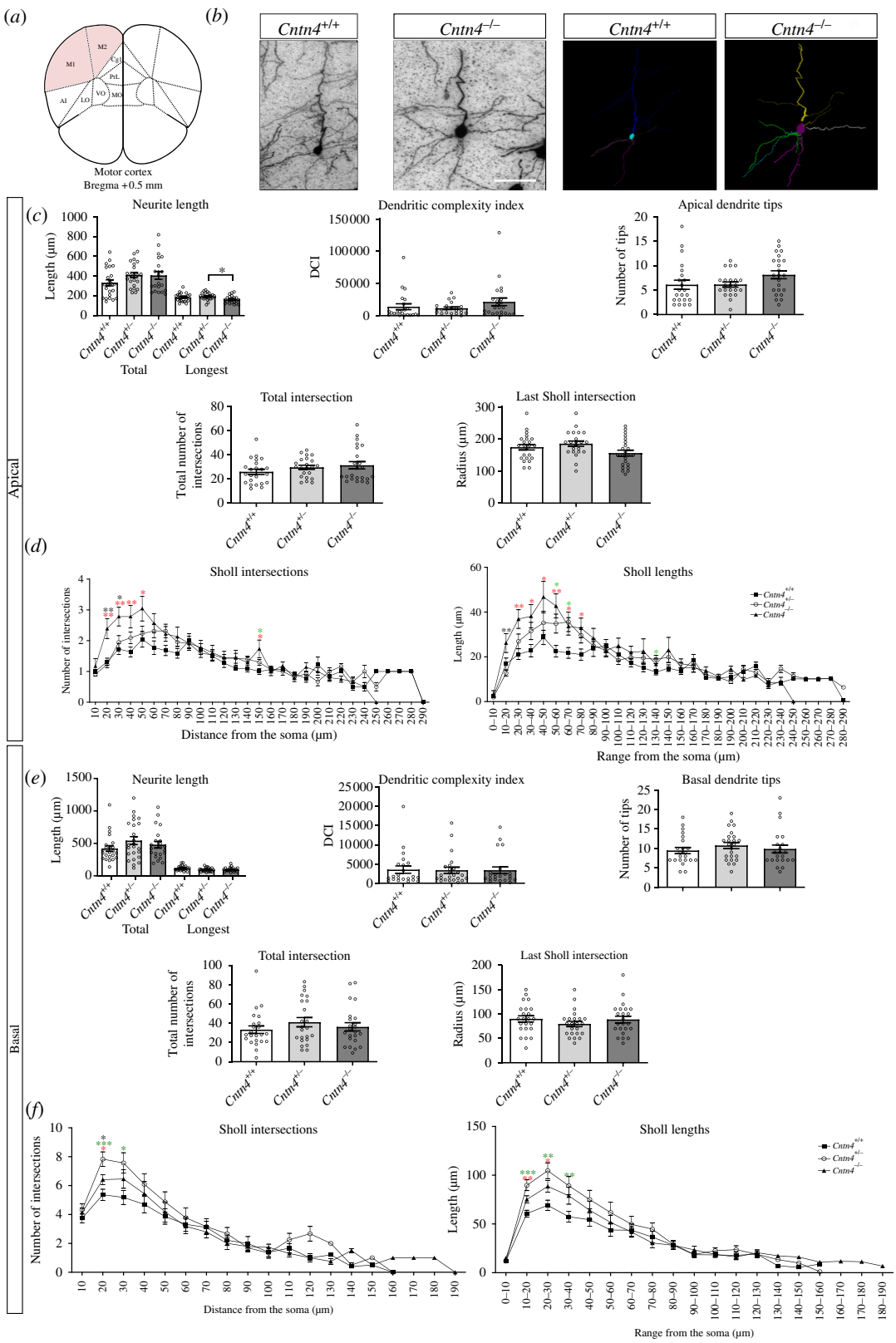

Figure 2. Neuron morphology analysis results for *Cntn4*$^{+/+}$, *Cntn4*$^{+/-}$ and *Cntn4*$^{-/-}$ mice primary motor cortex, layers II–III. (*a*) Schematic representation of the motor cortex with labelled Bregma anterior–posterior. (*b*) Golgi staining in *Cntn4*$^{+/+}$ and *Cntn4*$^{-/-}$ mice motor cortex and trace outlines of example pyramidal neurons. The scale bar represents 40 µm. (*c e*) Quantitative morphological results for the apical and basal dendrites, respectively. (*d f*) Sholl plots indicate the distribution of respective apical and basal dendritic intersections and length at increasing distance from the centre of the cell body. Quantitative analysis was performed, in each area, on at least three slices in *Cntn4*$^{+/+}$, *Cntn4*$^{+/-}$ and *Cntn4*$^{-/-}$ mice (n = 5 per genotype) using one-way ANOVA. Data are presented as mean ± s.e.m., cell number n = 23 (*Cntn4*$^{+/+}$), $n = 22$ (*Cntn4*$^{+/-}$), $n = 23$ (*Cntn4*$^{-/-}$) ($p = 0.0245$, *Cntn4*$^{+/-}$ versus *Cntn4*$^{-/-}$, longest apical neurite length). Red asterix corresponds to *Cntn4*$^{+/+}$ versus *Cntn4*$^{-/-}$, green asterix corresponds to *Cntn4*$^{+/+}$ versus *Cntn4*$^{+/-}$ and black asterix corresponds to *Cntn4*$^{-/-}$ versus *Cntn4*$^{+/-}$, $p < 0.05$.

2.7. Binding and *cis/trans* interactions between CNTN4 and APP

The SAINT and FC probability scoring confirmed APP as an interactor of CNTN4 (which has been previously described [53]), which we further examined *in vitro*. To validate the association of CNTN4 and APP, HEK293 cells were transfected with empty

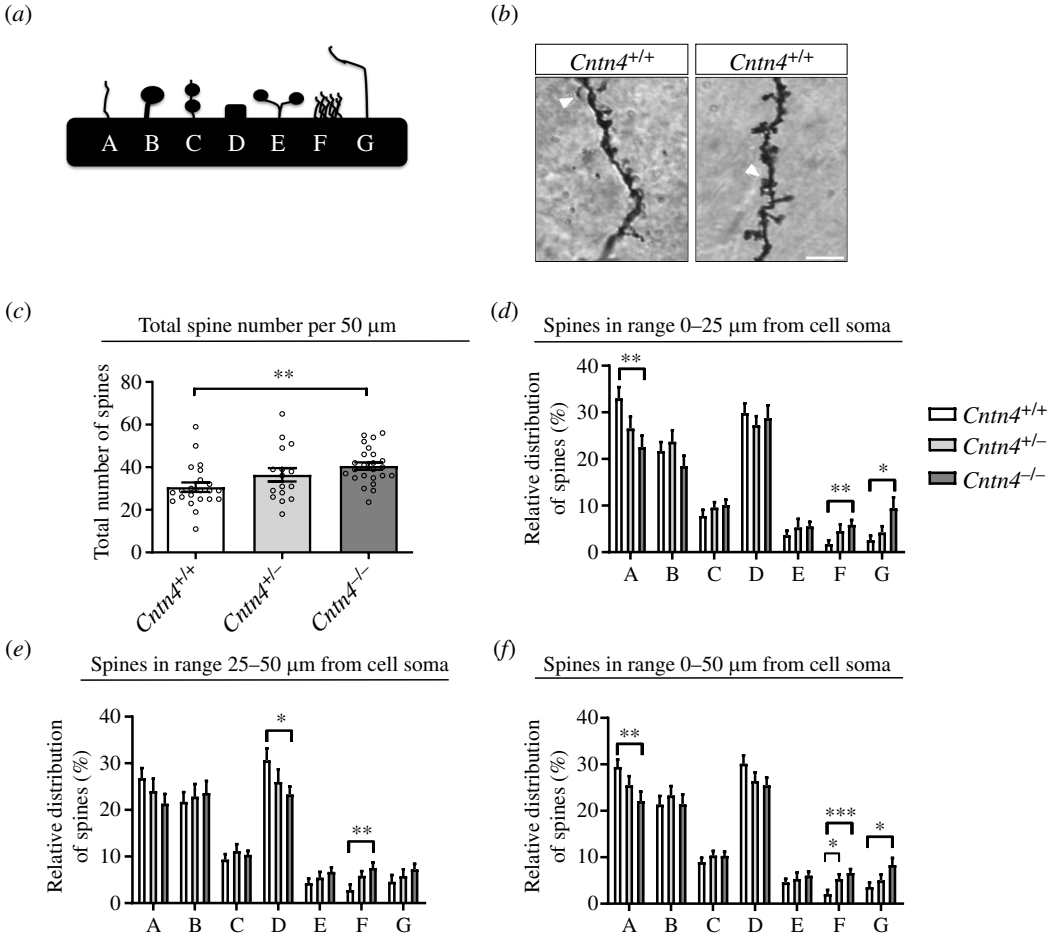

Figure 3. Spine analysis of M1 region, layers II–III pyramidal cells of adult *Cntn4*$^{+/+}$, *Cntn4*$^{+/-}$ and *Cntn4*$^{-/-}$ mice. (*a*) Schematic representation of different spine morphology categories, A = thin; B = mushroom; C = double mushroom; D = stubby; E/F/G = abnormal. (*b*) Golgi staining in *Cntn4*$^{+/+}$ and *Cntn4*$^{-/-}$ mice motor cortex of apical dendrites. The scale bar represents 5 µm. The arrowheads show example spine morphologies (category A in *Cntn4*$^{+/+}$ image and category F in *Cntn4*$^{-/-}$ image). Quantitative analysis reveals the (*c*) total number of spines and relative expression of the maturation state of spines in (*d*) first 25 µm; (*e*) final 25 µm and (*f*) total 50 µm. Analysis was performed on at least five mice for neurons, $n = 22$ (*Cntn4*$^{+/+}$), $n = 16$ (*Cntn4*$^{+/-}$), $n = 24$ (*Cntn4*$^{-/-}$) using one-way ANOVA. Data are presented as mean ± s.e.m.

or native CNTN4 expression plasmids. IP analysis by Western blotting demonstrated co-precipitation of CNTN4 and APP but not with control (figure 6*a*).

Investigating the cellular localization of the two proteins in cell lines and neuronal cultures further supported the interaction of CNTN4 and APP. Native CNTN4 transfected in HEK293 cells and endogenous APP co-localized on the membrane of the same cell (figure 6*b*), although the majority of APP was localized intracellularly. Similarly, immunostaining of cultured cortical neurons with anti-CNTN4 and anti-APP antibodies revealed endogenous localization of these proteins throughout the neurons (figure 6*c*). CNTN4 and APP were not clearly delineated on membranes of neurons and the bulk of the proteins seemed to localize intracellularly. Along the neurites, both CNTN4 and APP were expressed in puncta, of which some overlap. These results showed that CNTN4 and APP partly co-localize on the cell membrane when co-expressed. To study whether CNTN4 and APP interact in *cis* or *trans*, cell adhesion assays were performed (figure 6*d*). Separate populations of HEK293 cells were co-transfected either with CNTN4 together with DsRed or with APP together with EGFP expression plasmids. As a positive control, cells were co-transfected with NLGN1 and DsRed or with NRXN1β^{-} and EGFP expression plasmids. NLGN1 and NRXN1β^{-} are well-established *trans*-binding partners [54,55]. Since CNTN4 can form homodimers in *trans* [56], cells were also co-transfected with CNTN4 and EGFP or Cntn4 with DsRed expression plasmids, as a second positive control. As a negative control, cells were transfected with either DsRed or EGFP expression plasmids. Cells expressing DsRed, NRXN1β^{-} or APP, were incubated with cells expressing EGFP, NLGN1 or CNTN4. As a negative control, cells expressing DsRed were incubated with cells expressing EGFP. Cell aggregation was measured and quantified after incubating the cell mixtures for up to 90 min (figure 6*e*). A significant number of adhering cell clumps was observed when NRXN1β^{-}-expressing cells (green) were incubated with NLGN1-expressing cells (red), serving as a positive control. A significant degree of cell-aggregation was also observed in the mixture of CNTN4-expressing cells (green) with CNTN4-expressing cells (red), demonstrating CNTN4's capability of homodimerization [56]. It was observed that CNTN4-expressing cells (red) aggregated with APP-expressing cells (green) to a similar degree as the positive interaction between NRXN1β^{-}- and NLGN1-expressing cells. All three test conditions showed significant aggregation compared with the negative control. These data demonstrate that the binding of CNTN4 and APP can occur when the proteins are expressed on opposing cells in *trans* configuration but cannot rule out *cis* interaction as well. Subsequently, the cell surface binding assay [50] was performed that confirmed the *cis*-biochemical interaction between CNTN4 and APP. The binding between soluble, tagged APP-GFP and membrane-bound FLAG-CNTN4 was measured in HEK293 cells

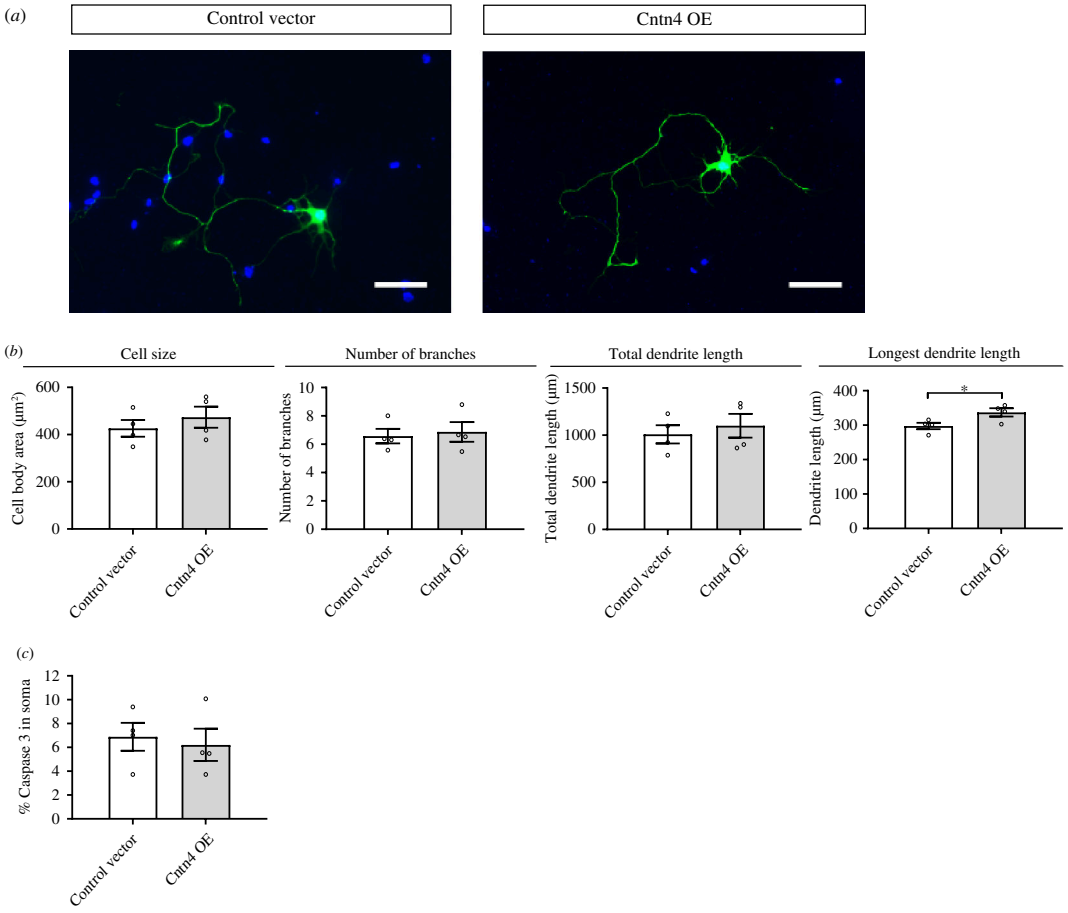

Figure 4. Primary culture of postnatal cortical neurons transfected with *Cntn4* or an empty vector after 48 h. Cortical cultures were prepared from mouse cortices at age P0–P1. Neurons were transfected with a control (empty) vector or *Cntn4* on DIV2. (*a*) Representative images of the morphology of *Cntn4* OE and empty vector-transfected neurons. Expression detected by anti-GFP (green) and DAPI (blue) staining. The scale bar represents 50 µm. (*b*) Average cell body surface in *Cntn4* OE and empty vector-transfected neurons; the total number of dendritic branches; total length of dendritic branches and length of the longest dendrite ($p = 0.0415$, unpaired Student's *t* test). Data are presented as mean ± s.e.m., four batches, total analysed cell number $n = 439$ (*Cntn4*$^{+/+}$), $n = 279$ (empty vector). (*c*) Quantification of the percentage of Caspase-3 positive neurons shows no significant difference between the control and *Cntn4* OE ($p > 0.05$, unpaired Student's *t* test, $n = 427$ total neurons analysed). OE, overexpression.

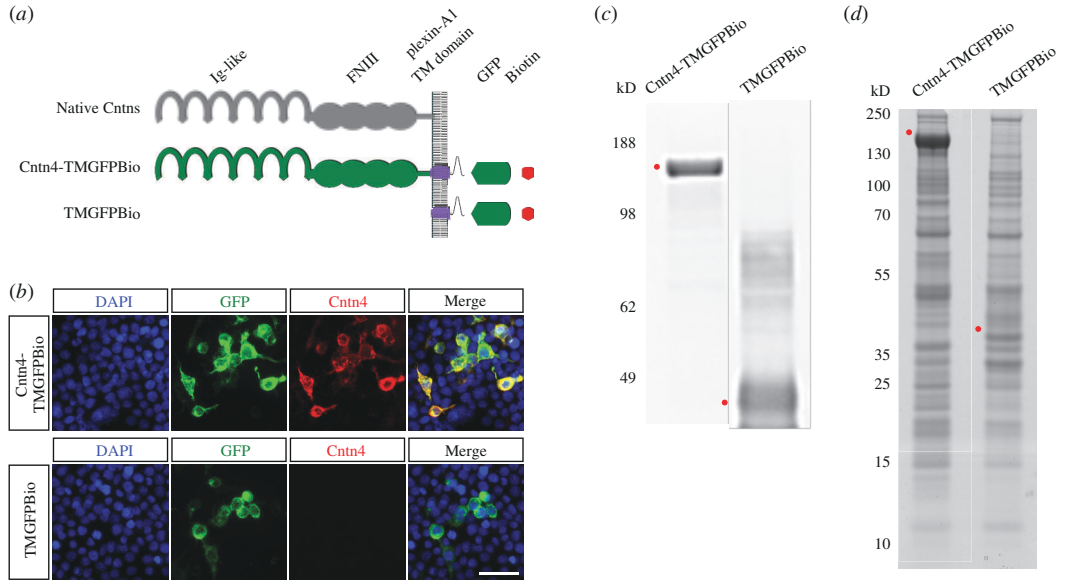

Figure 5. Identification of Cntn4 binding partners by proteomics. (*a*) The architecture of the native Cntn4 protein and the structures of the Cntn4 and control fusion proteins tagged with GFP and biotin. (*b*) Precipitations were performed by anti-GFP-coupled beads and eluates from anti-GFP-coupled beads were analysed on Western blot using an anti-GFP antibody. (*c*) Coomassie blue stained the NuPage 4–12% gels, which were submitted to mass spectrometry analysis. (*d*) Expression of Cntn4-TMGFPBio and TMGFPBio in HEK293 cells, detected by fluorescence (green), anti-Cntn4 antibody (red) and DAPI (blue) staining. Scale bar represents 30 µm. Red dots indicate respective expressed fusion proteins. Molecular weights are as follows: Cntn4-TMGFPBio = 147.8 kDa; TMGFPBio = 39.6 kDa. Bio, biotin; FNIII, fibronectin type III; GFP, green fluorescent protein; Ig-like, immunoglobulin-like; TM, transmembrane domain.

Table 1. Top CNTN4 interacting proteins.

PROTID	gene	FC-A	FC-B	SAINT	protein	cellular localization
P27797	*CALR*	10.33	8.12	1.0	calreticulin	endoplasmic reticulum; cytoplasm, extracellular space
Q62845	*Cntn4*	412.78	323.63	1.0	contactin-4	cell membrane
Q9UHD8	*SEPT9*	6.2	5.32	0.84	septin-9	cytoskeleton
Q13409	*DYNC112*	3.12	3.11	0.79	cytoplasmic dynein 1 intermediate chain 2	cytoskeleton
P35241	*RDX*	4.32	3.9	0.75	radixin	cell membrane; cytoskeleton
P12081	*HARS*	5.76	4.16	0.72	histidine-tRNA ligase, cytoplasmic	cytoplasm
Q8WU90	*ZC3H15*	4.45	3.4	0.71	zinc finger CCCH domain-containing protein 15	cytoplasm; nucleus
O75521	*EC12*	3.23	3.02	0.7	enoyl-CoA delta isomerase 2, mitochondrial	mitochondrion; peroxisome
P15311	*EZR*	3.36	3.0	0.7	ezrin	cell membrane; cytoskeleton
P51114	*FXR1*	3.45	3.28	0.69	fragile X mental retardation syndrome-related protein 1	cytoplasm
P63173	*RPL38*	6.19	4.69	0.69	60S ribosomal protein L38	cytoplasm
O43237	*DYNC1L12*	3.08	2.8	0.68	cytoplasmic dynein 1 light intermediate chain 2	cytoskeleton
P62273	*RPS29*	3.08	2.8	0.68	40S ribosomal protein S29	cytoplasm
P08670	*VIM*	5.7	2.19	0.67	vimentin	cytoplasm
O43707	*ACTN4*	11.91	4.43	0.67	alpha-actinin-4	cytoplasm; nucleus
Q5RKV6	*EXOSC6*	3.17	3.11	0.66	exosome complex component MTR3	cytoplasm; exosome, nucleus
Q16181	*SEPT7*	13.17	5.43	0.66	septin-7	cytoplasm, cytoskeleton, centrosome, cilium
P05067	*APP*	12.98	5.76	0.66	amyloid-beta precursor protein	cell membrane; amyloid
P80723	*BASP1*	5.17	3.75	0.66	brain acid soluble protein 1	cell membrane; growth cone
Q9UQE7	*SMC3*	4.4	3.16	0.66	structural maintenance of chromosomes protein 3	nucleus, centrosome
P35609	*ACTN2*	3.46	2.8	0.66	alpha-actinin-2	cytoplasm

Notes. The proteins that were co-immunoprecipitated with Cntn4-TMGFPBio and detected by mass spectrometry are listed according to their SAINT score. Data from triplicate IPs were compared with control using CRAPome, which employs SAINT and FC statistical analyses. This table lists the protein identification code (PROTID) and its related gene name, together with FC-A, FC-B and SAINT scoring. The standard CRAPome Fold Change calculations (FC-A) estimate the background by averaging the spectral counts across the selected controls. Another more stringent Fold Change (FC-B) calculation estimates the background by combining the top three values for each identified interacting protein, while SAINT reports a probability of true interaction. Cellular localization was determined by searching Uniprot [52]. See the Supplementary Proteomics Datasheet for the complete raw data.

via confocal microscopy (figure 6*g*, lower panel). The well-characterized *trans*-interacting proteins neogenin and RGMa were used as positive controls in this assay (figure 6*g*, top panel). Quantification shows a significant number of double-labelled transfected cells in the condition of CNTN4 and APP (figure 6*h*), which confirms a *cis* interaction between CNTN4 and APP.

2.8. *APP* deficiency causes abnormal apical dendrite morphology

Since the CNTN4–APP interaction suggested an involvement of APP in the pyramidal neuron phenotypes of cortical neurons, we investigated the morphology of Golgi-stained pyramidal neurons in $App^{+/+}$, and $App^{-/-}$ mice (figure 7*a,b*). Pyramidal neurons in the motor cortex layers II–III were analysed for dendrite length, branching and complexity. There were no significant differences in apical or basal neurite length, DCI, total intersection number and last Sholl intersection (figure 7*c,e*). However, there were significant morphological changes in the apical dendrite, since the number of apical dendrite tips was significantly decreased in the $App^{-/-}$ mice compared with the $App^{+/+}$ mice ($p = 0.0276$, $App^{+/+}$ versus $App^{-/-}$, unpaired Student's t test) (figure 7*c*).

Sholl plots indicated the distribution of dendritic intersections and length at increasing distance from the centre of the cell body. The $App^{-/-}$ mice had significantly fewer Sholl apical intersections in the range of 220–250 µm from the soma compared with $App^{+/+}$ mice. Furthermore, significantly shorter Sholl apical lengths in the range of 210–230 µm from the soma were observed in $App^{-/-}$ mice (figure 7*d*). Taken together, the morphological changes in pyramidal neurons, as observed in $Cntn4^{-/-}$, were not observed in $App^{-/-}$.

2.9. Expression levels and morphology of CNTN4- and APP-deficient human cells

The neuroblastoma cell line SH-SY5Y is a well-established model for the differentiation of cells into cortical-like neurons [58,59] and was used to evaluate the single and double loss-of-function of CNTN4 and APP on neuronal differentiation *in vitro*.

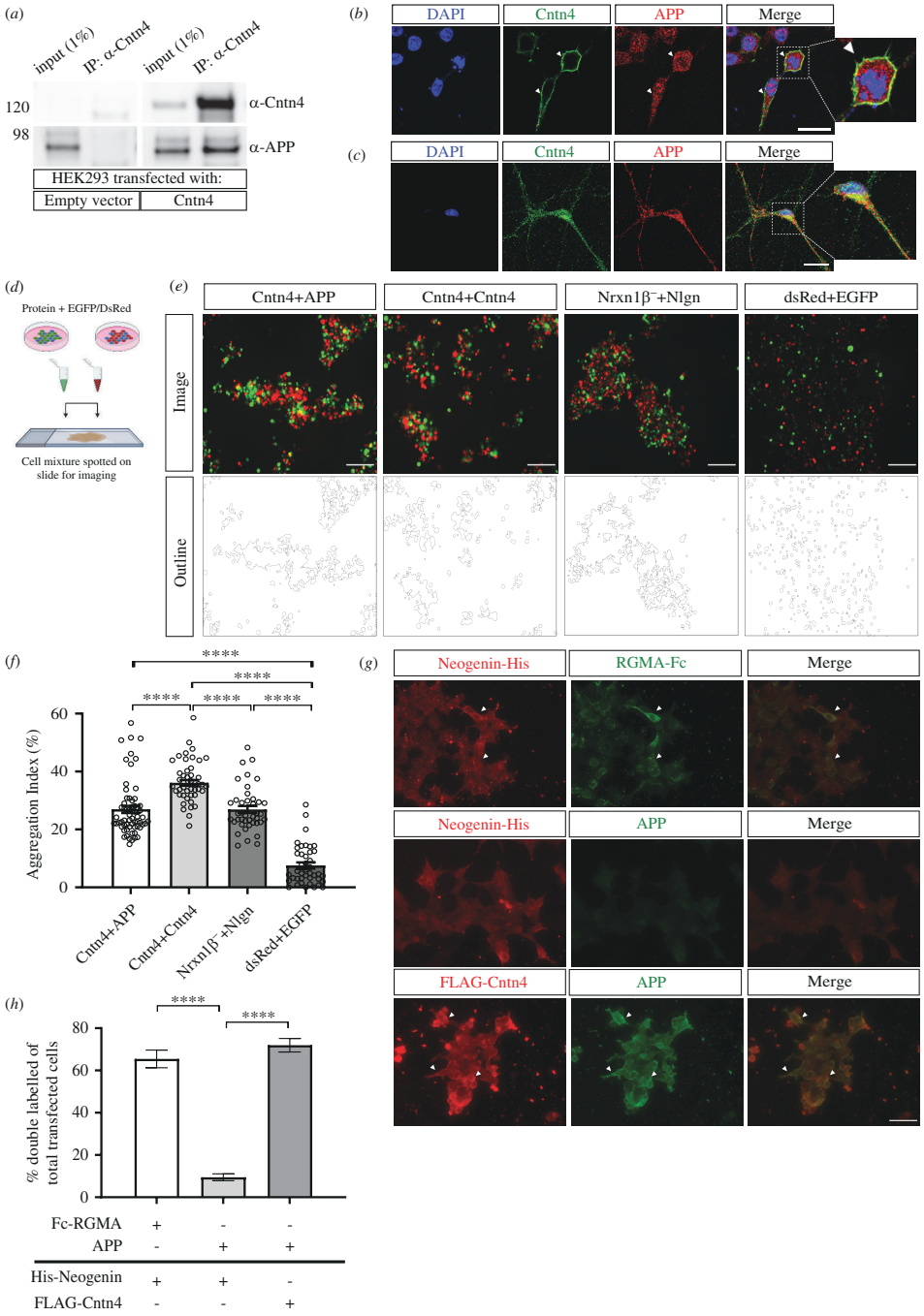

Figure 6. Interaction of CNTN4 and APP. HEK293 cells were transfected with an empty vector or CNTN4 expression plasmid, coding for the native Cntn4 protein. (*a*) After IP of the CNTN4 by an anti-CNTN4 antibody, the eluates were analysed by Western blot. Blots stained with antibodies against CNTN4 and APP revealed an interaction between CNTN4 and APP. No co-precipitation was found in normal IgG control IP. (*b*) HEK293 cells expressing CNTN4 protein (green) co-localized with endogenous APP (red) on the membrane. Arrows indicate co-expression on the membrane. DAPI staining is in blue. The scale bar represents 20 µm. (*c*) Endogenous CNTN4 (green) and APP (red) are co-expressed in neurons. DAPI staining is in blue. The scale bar represents 20 µm. (*d*) Schematic overview of the cell adhesion assay, in which populations of HEK293 cells were co-transfected with different proteins and either EGFP or DsRed expression plasmids. Two HEK293 cell populations were combined and incubated. Cell suspensions were spotted onto slides for imaging by fluorescence microscopy. Created with BioRender.com. (*e*) Cells expressing either EGFP alone or together with NRXN1β^{-} or APP (green) were mixed with cells expressing DsRed alone or together with NLGN1 or CNTN4 (red). Aggregation of cells expressing NRXN1β^{-} + EGFP with NLGN1 + DsRed, CNTN4 + EGFP with CNTN4 + DsRed and CNTN4 + DsRed with APP + EGFP was observed. There was no aggregation of cells expressing EGFP + DsRed. The scale bar represents 200 µm. (*f*) Aggregation index was determined from five fields of 1.509 mm^2 per cell suspension combination of each independent cell adhesion assay ($n = 3$). Analysis was performed using one-way ANOVA. The graph bars are presented as mean ± s.e.m. ****$p < 0.0001$. (*g*) HEK293 cells expressing Neogenin-His or FLAG-CNTN4 were incubated with soluble ecto-domains of RGMA-Fc and APP. Upper panel: Neogenin-His-expressing cells (red) bound soluble RGMA-Fc (green), but not with APP (green) (middle panel). Lower panel: FLAG-CNTN4-expressing cells (red) bound soluble APP (green). Scale bar represents 50 µm. Arrowheads indicate examples of green and red overlay. (*h*) Quantification of about 300 transfected cells per transfection condition of each independent cell surface binding assay ($n = 3$) was performed. Statistical analysis was performed using unpaired Student's *t* test and one-way ANOVA. The graph bars are presented as mean ± s.e.m. ****$p < 0.0001$. APP, amyloid-precursor protein.

CNTN4$^{-/-}$, *APP*$^{-/-}$ and *CNTN4*$^{-/-}$/*APP*$^{-/-}$ SH-SY5Y neuroblastoma cell lines were generated by CRISPR-Cas9 gene editing (figure 8*a*,*c* and electronic supplementary material). A cell line created by transfection of empty CRISPR vector was used as a control cell line (EV). Reverse transcription (RT-PCR) was performed on all knockout cells with primers designed for targeting *CNTN4*

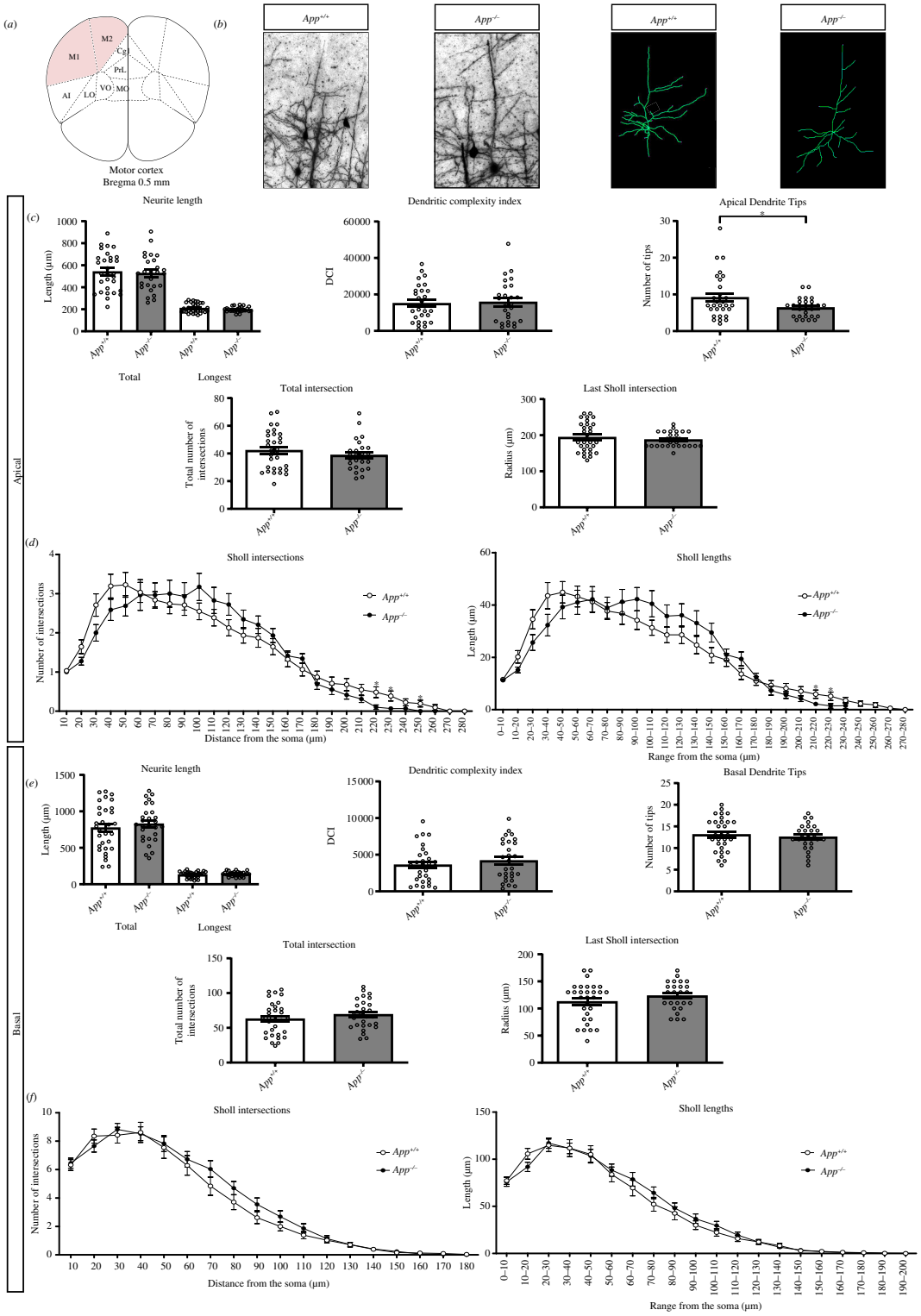

Figure 7. Neuron morphology analysis results for the primary motor cortex. (*a*) Schematic representation of the motor cortex with labelled Bregma anterior–posterior. Adapted from [57]. (*b*) Golgi staining in $App^{+/+}$ and $App^{-/-}$ mice motor cortex and trace outlines of example pyramidal neurons. The scale bar represents 40 µm. (*c,e*) Quantitative morphological results for the apical and basal dendrites, respectively. (*d,f*) Sholl plots indicate the distribution of respective apical and basal dendritic intersections and length at an increasing distance from the centre of the cell body. Quantitative analysis was performed, in each area, on at least six slices in $App^{+/+}$ and $App^{-/-}$ mice ($n = 5$ per genotype). Data are presented as mean ± s.e.m., cell number $n = 30$ ($App^{+/+}$), $n = 30$ ($App^{-/-}$). ($p = 0.0276$, $App^{+/+}$ versus $App^{-/-}$, apical dendrite tips). Statistical analyses were carried out using unpaired Student's *t* test. APP, amyloid-precursor protein.

and *APP* (figure 8*d,e*). mRNA expression levels of *Cntn4* were found to be significantly reduced by approximately 50% in the $APP^{-/-}$ SH-SY5Y cell line, relative to EV expression levels. Conversely, mRNA expression levels of *APP* were reduced by approximately 50% in the $CNTN4^{-/-}$ and EV SH-SY5Y cells. As expected, both *CNTN4* and *APP* mRNA expression levels were reduced in the $CNTN4^{-/-}/APP^{-/-}$ SH-SY5Y cells. Levels of *Cntn4* and *App* mRNA expression levels were also determined in the respective $Cntn4^{-/-}$ and $App^{-/-}$ mouse models compared with wild-type mice (see electronic supplementary material, figure S3). mRNA expression levels of *App* were reduced by approximately 25% in the $Cntn4^{-/-}$ mouse cortex; however, there was no significant change in the mRNA expression levels of *Cntn4* in the $App^{-/-}$ cortex.

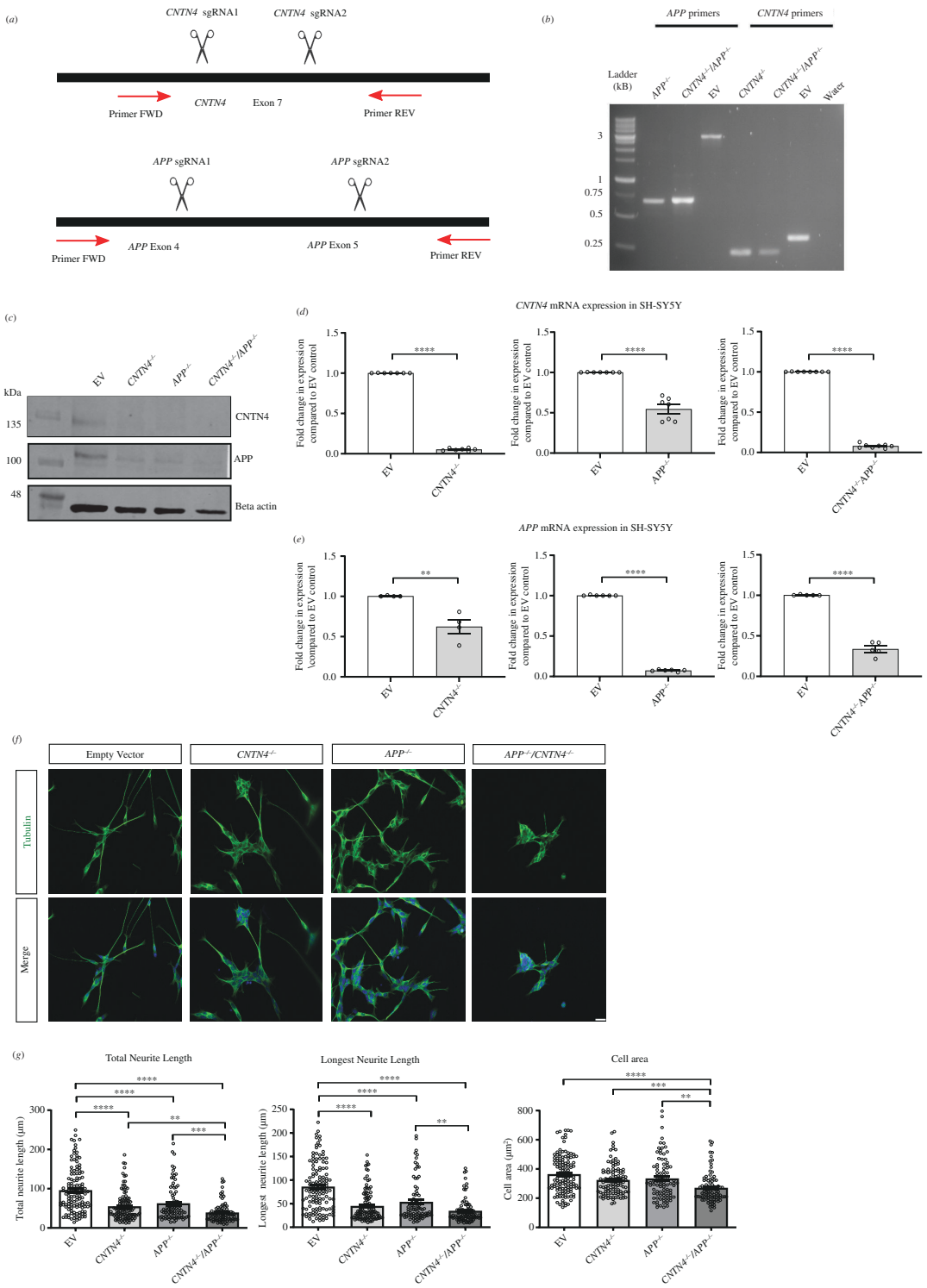

Figure 8. CNTN4 knockout cell lines show morphological differences and significantly higher levels of apoptotic activity. (*a*) Schematic representation of the sgRNA designed to cause an indel in *CNTN4* and *APP*, respectively. (*b*) SH-SY5Y clonal cells were screened via PCR using specific primers for *CNTN4* and *APP.* EV = empty vector control. Expected sizes were for APP EV = 2.905 kB, APP knockout = 0.701 kB, CNTN4 EV = 0.341 kB, CNTN4 knockout = 0.249 kB. 1 kB ladder (Solis Biodyne). (*c*) Protein extracted from SH-SY5Y cells was analysed by Western blot. Blots stained with anti-CNTN4 and anti-APP antibodies revealed lower expression in *CNTN4*$^{-/-}$, *APP*$^{-/-}$, *CNTN4*$^{-/-}$/*APP*$^{-/-}$ cells, respectively. Western blotting was performed on four SH-SY5Y cell lines (empty vector, *CNTN4*$^{-/-}$, *APP*$^{-/-}$, *CNTN4*$^{-/-}$/*APP*$^{-/-}$). Molecular weights are as follows: CNTN4 = 150 kDa; APP = 100–140 kDa; beta-actin = 47 kDa. (*d*) Fold change of *CNTN4* and (*e*) *APP* expression levels in *CNTN4*$^{-/-}$, *APP*$^{-/-}$, *CNTN4*$^{-/-}$/*APP*$^{-/-}$ cells compared with empty vector cells, generated by qRT-PCR. Analysis was performed on three SH-SY5Y cell lines (*CNTN4*$^{-/-}$, *APP*$^{-/-}$, *CNTN4*$^{-/-}$/*APP*$^{-/-}$) using one-way ANOVA and Tukey's multiple comparison post hoc test. Primer sets *Cntn4* P2 and *App* P4 are presented, but two further primer sets are presented in electronic supplementary material, figure S2. All primer detail is included in the electronic supplementary material. (*f*) Representative images of the morphology of empty vector, *CNTN4*$^{-/-}$, *APP*$^{-/-}$ and *CNTN4*$^{-/-}$/*APP*$^{-/-}$ cells. Tubulin staining is in green and DAPI staining is in blue. The scale bar represents 25 µm. (*g*) Quantitative morphological analysis was performed on at least three coverslips in empty vector, *CNTN4*$^{-/-}$, *APP*$^{-/-}$ and *CNTN4*$^{-/-}$/*APP*$^{-/-}$ cells ($n = 3$ per genotype). Data are presented as mean ± s.e.m., cell number $n = 30$ per genotype. *$p < 0.05$. **$p < 0.01$. ***$p < 0.001$. ****$p < 0.0001$. Statistical analyses were carried out using unpaired Student's *t* test.

Knockout SH-SY5Y cells were differentiated using retinoic acid, BDNF and lack of FBS over a 5-day period, adapted from Shipley *et al.* [60]. Morphological analysis was carried out on differentiated cells. It was observed that the total and longest neurite length was significantly reduced in the *CNTN4*$^{-/-}$, *APP*$^{-/-}$ and *CNTN4*$^{-/-}$/*APP*$^{-/-}$ cells compared with the EV cells (figure 8*f*,*g*). It was further observed that the cell area was significantly reduced in the *CNTN4*$^{-/-}$, *APP*$^{-/-}$ and *CNTN4*$^{-/-}$/*APP*$^{-/-}$ cells compared with the EV cells (figure 8*f*,*g*). This suggests that the interaction between CNTN4 and APP contributes to their gene expression and contribution to neurite outgrowth.

3. Discussion

We have shown that *Cntn4*-deficient mice have abnormalities in the motor cortex. This is important since CNTN4 has previously been associated with neurodevelopmental disorders such as ASD [28,36,37]. To understand the aetiology of disorders such as ASD, and the role that CNTN4 has, we set out to examine the pathological effects of loss-of-function of this Contactin family member. The loss of *Cntn4* does not affect gross anatomical development, such as body weight and brain size in mice [44].

Cntn4-deficient mice have significantly reduced cortical thickness in the M1 motor cortex region and altered dendrite length and complexity in M1 neurons. We interpret that CNTN4 has a specific role for the M1 region, supported by the absence of effects in other cortical areas (see electronic supplementary material, figure S1). In addition, APP/APLP2 NexCre cDKO mice show a small reduction in hippocampal volume due to a reduction in the dendritic complexity of neurites [61]. The motor cortex is in close proximity to the main olfactory bulb and accessory olfactory bulbs, and these respective regions have shown CNTN4 to be an axon guidance molecule that mediates neuronal wiring [62]. Kaneko-Goto *et al.* demonstrated the importance of CNTN4 in organizing the wiring of the olfactory system, where CNTN4 deficiency leads to aberrant connections of the neurons to the olfactory receptors [41]. Our research revealed comparable findings in the M1 region since *Cntn4*-deficient mice revealed abnormal cell outgrowth and arborization in proximity to the cell soma, and increased dendrite length (figure 2). This suggests a role for CNTN4 in dendrite outgrowth and directionality in the M1 motor cortex.

Disrupted neuron migration, abnormal neurite growth and spine formation in the cortex are all associated with neurodevelopmental disorders such as ASD [63,64]. *Cntn4*-deficient mice demonstrate decreased cortical thickness in the motor region, abnormal spine density and decreased length of the longest neurite (figures 1–3). The latter is also in agreement with human *CNTN4*$^{-/-}$ SH-SY5Y cell morphology (figure 8*g*). Moreover, OE of CNTN4 in cortical neurons causes an increased length of the longest neurite but no significant change in apoptosis (figure 4). These morphology and apoptosis results agree with previous reports of CNTN6 OE in cortical neurons [50] and CNTN4-6 OE co-culture experiments of rat cortical neurons and HEK293 cells [65]. Cell adhesion molecules such as CNTNAP2 and Contactin family members are known to play crucial roles in neuritogenesis [65,66], and deficits such as abnormal cortical migration in the *Cntnap2*$^{-/-}$ mouse model have been linked to ASD [67].

Spines contain a range of proteins amongst which receptors, cytoskeletal and adaptor proteins, and associated signalling molecules [68] are dynamic in response to synaptic activity [69]. Kaneko-Goto *et al.* identified that CNTN4 expression is regulated by neuronal activity [62] and Zhao *et al.* found enriched expression of CNTN4 at excitatory synapses on dendritic spines [70]. *Cntn4*-deficient mice showed an increased spine density in cortical neurons (figure 3), suggesting CNTN4 is not required for the formation of cortical spines. Interestingly, Zhao *et al.* observed that knockdown of CNTN4 by shRNA transfection reduced the spine density of primary cortical neurons in culture [70], whereas the present results were the opposite of these findings. This suggests some brain area-specificity in the mouse brain may be altering the cascade that contributes to the formation of spines. In further contrast, the spine density in hippocampal neurons decreased with *Cntn4* deficiency [44], pointing towards a cell type-specific role for CNTN4. It was further observed that there were less immature and more abnormal cortical spines found in the absence of *Cntn4*, suggesting an important role in synapse quality. This suggests that while *Cntn4* contributes to spine formation in the cortex and hippocampus, it has an alternative role in the spine formation process. Spine maturity is suggested to be the subject of glutamate receptor input [69,71] and, as a consequence, influences the excitation–inhibition balance. Previous reports observed that a disruption in CNTN4 causes a decrease in the number of excitatory synapses and therefore a decrease in neural activity [70]. Our data also suggest a role for *Cntn4* in the maturation of spine development, which may influence the excitation–inhibition balance and contribute to the stability of the synapse after formation. The role of dysregulated CNTN and CNTNAP at the synapse has been previously postulated [72].

The question is whether CNTN4 deficiency alone is causal of the abnormalities or that CNTN4 is part of a crucial interaction. To answer this, binding assays were carried out to reveal the interacting partners of CNTN4 and understand their function. Osterfield *et al.* [53] showed that CNTN4 and APP were direct binding partners, which we confirm through our independent unbiased proteomics screen (figure 5 and table 1) and binding assays (figure 6). In this study, CNTN4 appeared to be bound to full-length APP, since the tryptic peptides found in mass spectrometry were derived from full-length APP and co-IP validated this interaction between CNTN4 and APP (figure 6). APP is known to be involved in *cis* and *trans*-cellular adhesion [73] and is a synaptic adhesion molecule [74,75]. CNTN4 and APP may stabilize one another at the cell surface, which is subsequently important for synaptogenesis.

Osterhout *et al.* observed that in the absence of CNTN4 or its binding partner APP, deficiencies were observed in the developing chick retinotectal system [42,76]. APP, a transmembrane protein, is unquestionably associated with Alzheimer's disease but also serves crucial physiological functions [46] for neuronal migration, neuronal morphology, synaptic plasticity, learning and memory [61], and more recently also for ASD-like abnormalities [77]. The interaction between Contactin family members, including CNTN4, and APP has been reviewed elsewhere [72]. In particular, APP is highly expressed in the developing cortex during differentiation and migration of cortical neurons [78–80]. Osterfield *et al.* demonstrated that the soluble

isoform of CNTN4 is secreted by neurons, and creates a gradient upon which dendrites can grow [53]. This agrees with our finding that OE of CNTN4 in primary neurons resulted in significantly longer dendrites (figure 4). Similarly, Osterfield *et al.* showed that APP also promoted neurite outgrowth [53]. Given the parallels between CNTN4 and APP, interestingly, the *App*$^{-/-}$ mice had a mild phenotype, and there was little evidence of morphological abnormality (figure 7) and change in *Cntn4* mRNA expression levels. More pronounced effects are observed in aged *App*$^{-/-}$ mice, in the spine density and dendritic branching of CA1 and LII-III neurons [81]. Results in the *App*$^{-/-}$ mice cannot be attributed solely to any interaction APP may have with CNTN4. Compensation by other family members such as APLP1 and APLP2 is discussed later; however, it is worth noting here that the phenotype of the combined double and triple KO mutants of the APP family is much more severe than the single APP KO [61,77]. Furthermore, APP itself regulates many genes [82], and there are many genes which regulate the process of APP cleavage [83], and therefore, it would be of future benefit to investigate the genes responsible for regulating APP gene expression, for example, the downregulation of two genes PSMA5 and PSMB7 involved in APP-induced cell proliferation impairment [84].

CNTN4 also interacts through its Ig-like domains with PTPRG, which is expressed primarily in the nervous system and mediates cell adhesion and signalling events during development [85,86]. We did not further investigate this interaction since PTPRG was not identified in our proteomics screen. Additionally, Mercati *et al.* found differences in neurite outgrowth were not caused by the CNTN4 and PTPRG interaction [65]. Candidate proteins identified to be APP binding partners include F-spondin [87], collagen, netrin-1, laminin and the Aβ peptide [88]. APP has been shown to have a direct high-affinity interaction with contactin 3 and 4 [53]. Additionally, adhesion proteins such as neurexin have been shown to have functional interaction with APP [89]. In functional assays of cultured retinal ganglion cells, CNTN4 and APP modulated axon behaviour specifically in the context of NgCAM-dependent axon growth, demonstrating functional interactions among these proteins.

In order to investigate mediating effects, studies of CNTN4 and APP deficiency were carried out (figure 8 and electronic supplementary material, figure S3). There was no significant change in *Cntn4* mRNA expression levels in the *App*$^{-/-}$ mouse, but *App* mRNA expression levels were found to be lowered in the *Cntn4*$^{-/-}$ mouse (see electronic supplementary material, figure S3). CNTN4 mRNA and protein expression levels were significantly reduced in the *APP*$^{-/-}$ SH-SY5Y cell line, and vice versa APP mRNA, and protein levels were significantly reduced in the *CNTN4*$^{-/-}$ SH-SY5Y cell line (figure 8). It was evident from *in vitro* mRNA expression levels that CNTN4 and APP were dependent on one another, although we cannot say exclusively. Osterfield *et al.* demonstrated that CNTN4 had the highest binding affinity to APP [53], and we further observed that the interaction has approximately 50% impact on mRNA and protein levels, respectively. This suggests that a complex needs to be formed for mutual stability, and furthermore, the binding of CNTN4-APP can be functionally meaningful at around 50% of their protein levels. In addition, there were significant morphological deficiencies in all knockout SH-SY5Y cell lines compared with the EV control. The most severe morphological deficiencies were observed in the *CNTN4*$^{-/-}$/*APP*$^{-/-}$ SH-SY5Y cell line, which further emphasizes the importance of the CNTN4 and APP interplay.

The FnIII domain of CNTN4 is reported to interact with the E1 domain of APP, and other APP family members, on the cell surface [53,90]. Zhao *et al.* observed CNTN4 proteins lacking FnIII or GPI domains lack the ability to regulate dendritic spine formation [70]. Our hypothesis is that when CNTN4 is deficient there are two possibilities: (i) the function mediated by the binding of CNTN4 to APP is lost, and this, in turn, leads to a reduced ability of CNTN4 to regulate dendritic spine formation and abnormal neurite outgrowth; (ii) the loss of CNTN4 would cause other proteins to interact with the APP-E1 domain and thereby affect neurite outgrowth and arborization. For example, the arborization trends of the near and distal Sholl apical and basal dendrites are the opposite of one another in the *Cntn4*- and *App*-deficient mice, respectively. Loss of either CNTN4 or APP may activate these opposing scenarios through inhibition of signalling, binding to another partner or both. However, further studies are needed to understand the interplay. There is also the important consideration of the amyloidogenic and non-amyloidogenic APP processing pathways, and whether the lack of CNTN4 interaction might affect it. For example, APPsα is a cleaved ectodomain of APP, which has been shown to modulate cell behaviours including neurite outgrowth, synaptogenesis, neurogenesis, and cell survival and proliferation [91–93]. In this capacity, the interaction of CNTN4 with APP may have potential therapeutic effects. In the case of APP deficiency, CNTN4 is hypothesized to show more prominent binding to other APP family members, such as APLP1 or APLP2, which also harbour a highly conserved E1 domain [94,95]. This, in turn, offers further therapeutic benefits, since APLP1 and APLP2 cannot generate an amyloidogenic fragment, since the membrane-proximal region of APP is not conserved in the APLPs. However, the physiological function of the other APP family members is not fully understood. Missense mutations in the APP gene have been shown to cause familial AD [96]. The physiological relationship between APP and Contactin members and their role in pathophysiology of AD is reviewed elsewhere [72]. Our data suggest that the interplay between CNTN4 and APP is important for synapse maintenance and neuronal stabilization.

This research identified structural abnormalities in the brains of *Cntn4*$^{-/-}$ mice. Reduced cortical thickness of the layers of the M1 region was identified, which echoes connectivity and phenotypic abnormalities observed in ASD patients. Brimberg *et al.* observed cortical thinning in male mice after administration of Contactin-associated protein Caspr2-reactive antibody cloned from the mother of an ASD child [97], which aligns with the gene-dosage-dependent cortical layer thinning in the motor cortex. Sensorimotor development impairments and ASD stereotypic motor movements have been previously observed in Pcdh9 and Cntnap2 knockout mouse models, respectively [67,98]. Motor abnormalities correlate with ASD severity and are persistent in child development as well as in adults clinically diagnosed with ASD [99–103]. Moreover, functional studies in human ASD patients suggest that subnetworks in the M1 region are alternatively activated in comparison with normal development and within equivalent age groups showed that motor impairments are caused by underlying structural abnormalities or abnormal connectivity within brain networks in the M1 cortex [104–107].

To summarize, our study identified differences in cell density and differentiation in the M1 region of CNTN4-deficient mice and a role for CNTN4 in neurite outgrowth and directionality. The interaction between CNTN4 and APP was also shown to be important in knockout human cell lines, with significant defects in cell morphology and elongation and the observation that CNTN4 mediates neurite outgrowth by binding to APP. This provides an important step forward in our understanding of Alzheimer's disease, ASD and this field of neuroscience. It will be important for future neuropsychiatric studies to clarify how precisely CNTN4 affects APP binding and whether it is involved in APP processing.

In conclusion, our study revealed variations in cell density and differentiation in the M1 region of CNTN4-deficient mice, along with CNTN4's role in guiding neurite growth and direction. The significance of CNTN4's interaction with APP was also confirmed in human cell lines lacking CNTN4, highlighting defects in cell structure and elongation. Notably, our findings suggest that CNTN4 facilitates neurite extension through its interaction with APP. This advancement enhances our comprehension of Alzheimer's disease, ASD and the broader neuroscience field. For forthcoming neuropsychiatric investigations, elucidating CNTN4's impact on APP binding and its involvement in APP processing will be pivotal.

4. Material and methods

4.1. Animals

Cntn4-deficient mice were kindly provided by Dr Yoshihiro Yoshihara (RIKEN, Japan) [62]. These mice were generated using a standard gene-targeting method as previously described. All experimental procedures were performed according to the institutional guidelines of the University Medical Center Utrecht. All animal procedures were performed according to NIH guidelines and approved by the European Council Directive (86/609/EEC). For further generation and genotyping details, see electronic supplementary material.

App knockout mice ($App^{-/-}$) and littermate wild types ($App^{+/+}$) were described previously [108]. Fresh brain tissue extracted from male, five-month-old mice was prepared as described in §4.4. RNA extraction, cDNA generation and real-time RT-PCR were performed on cortical tissue from 11-week-old $App^{-/-}$ (n = 5) and 10-week-old $App^{+/+}$ (n = 5) mice, as previously described [44].

4.2. Nissl staining

Brains were sectioned with a cryostat (Leica Microsystems, Wetzlar, Germany) coronally at 40 µm from rostral to caudal. Sections were mounted onto Superfrost slides (VWR, 631-0108). The slices were rehydrated in graded levels of decreased concentrations of alcohol and then stained in 0.5% Cresyl-Violet (Sigma Aldrich, 190-M) for 5 min. Finally, the slices were dehydrated in graded levels of increased concentrations of alcohol, cleaned in xylene and then cover-slipped using Entellan® (Merck, Damstadt, Germany, 107961).

Slices were imaged using light microscopy (Zeiss Axio Scope.A2, Germany) using the following stereotaxic coordinates [57]: Bregma anterior–posterior +0.5 mm (frontal motor cortex), −1.70 mm (primary somatosensory cortex) and −2.80 mm (visual cortex).

Analysis of cortical thickness was performed within the frontal motor cortex (+0.5 mm to bregma), primary somatosensory cortex (−1.70 mm to bregma) and visual cortex (−2.80 mm to bregma) in all used brains. For cortical layer thickness, the superficial (layers I–IV) and deeper layers (layers V and VI) were measured, in each area, on at least three slices in $Cntn4^{+/+}$ (n = 7), $Cntn4^{+/-}$ (n = 4) and $Cntn4^{-/-}$ mice (n = 4) using ImageJ software [109].

4.3. Immunohistochemistry

Brains were sectioned as described above and free-floating slices were stored in 0.02% sodium azide until immunohistochemistry was performed. The sections were washed with PBS and incubated in blocking buffer (1% BSA, 0.2% fish skin gelatin (Sigma Aldrich, G7765), 0.1% Triton X-100 in PBS) for 45 min. Sections were washed and incubated in permeabilization buffer (0.3% Triton X-100 in PBS) for 10 min before incubation with primary antibody in blocking buffer at 4°C for 2 h. The sections were washed in PBS and pre-incubated with blocking buffer before incubating with secondary antibody at room temperature (RT) for 2 h. The sections were embedded with polyvinyl alcohol mounting medium with DABCO® anti-fading (Sigma Aldrich, 10981) onto glass slides after additional PBS wash steps.

Immunohistochemistry primary antibodies were used as follows: Rabbit anti-Cux1 (1:250, Santa Cruz, sc-13024), mouse anti-NeuN (1:250, Millipore, MAB377) and DAPI. Appropriate secondary antibodies were used from the Molecular Probes Alexa Series (1:250, Invitrogen). Images were captured by confocal laser scanning microscopy (Zeiss Axio Scope A1, Germany) and image analysis was carried out in ImageJ software [109]. Areas assessed were found using the following stereotaxic coordinates [57]: Bregma anterior–posterior +0.5 mm (frontal motor cortex). Cell counting was performed (Cell Counter, ImageJ) in the frontal motor cortex. For the frontal motor cortex (M1), antibodies Cux1 and NeuN were used to stain pyramidal neurons in layers II–IV; pyramidal neurons in layers V–VI and neurons in general, respectively. Selected images comprised at least 20 randomly selected microscope fields in the designated layers (area 0.1 mm^2) from the motor cortex. In addition, DAPI staining allowed the total number of cells to be counted. An average measurement from at least six slices was performed in $Cntn4^{+/+}$ (n = 5), $Cntn4^{+/-}$ (n = 4) and $Cntn4^{-/-}$ mice (n = 4).

4.4. Golgi staining

Golgi staining was performed using a FD Rapid GolgiStain™ kit (FD NeuroTechnologies, Columbia, MD, PK401) according to the instructions of the manufacturer. After treatment with Golgi solutions A, B and C, brains were sectioned with a vibratome (Leica Microsystems, Wetzlar, Germany) coronally at 150 µm thickness from rostral to caudal. The slices were attached to gelatin-coated slides and stained with Golgi solutions D + E. Finally, the slices were dehydrated in graded levels of increased concentrations of alcohol, cleaned in xylene and then cover-slipped using Entellan®.

Slices were imaged using light microscopy (Zeiss Axio Scope A2, Germany). Areas assessed were found using the following stereotaxic coordinates [57]: Bregma anterior–posterior +0.5 mm (frontal motor cortex). Image analysis was carried out with Golgi microscope (Zeiss AxioImager M2, Germany) and Neurolucida software (MicroBrightField, Williston, VT). Further slices were imaged using light microscopy (Leica TCS SP8, Leica Microsystems, Mannheim, Germany).

Structural differences in spine number and spine morphology caused by *Cntn4*$^{-/-}$ mice were analysed as previously described [44], a total of 15 samples of different mice were included for final analysis: *Cntn4*$^{+/+}$, *Cntn4*$^{+/-}$, *Cntn4*$^{-/-}$ mice (n = 5 for each group). A total of 62 pyramidal neurons were included for final analysis (22 for *Cntn4*$^{+/+}$, 16 for *Cntn4*$^{+/-}$ and 24 for *Cntn4*$^{-/-}$ neurons). Thin, mushroom, stubby, abnormal and double mushroom spines were counted in the first 25 mm (50–75 mm) and second 25 mm (75–100 mm) of a branch of the proximal part of the apical dendrite (the first 1/3 part of the apical dendrite) in pyramidal neurons of the M1 region. The total number of spines includes all morphological categories. Neurolucida and Neuroexplorer software (Plexon, Dallas, TX), were used for the tracing of spines and analysis (spine number and spine morphology). The different spine morphology categories were counted. Primary branches at the proximal part (the first 1/3 of the apical dendrite) were included for spine analysis, and images acquired including circles with a diameter of 200, 150 and 100 µm from the branching place. Branches that were not long enough, or with branching places at the branch itself (between 100 and 200 µm) were excluded.

4.5. Neuronal cultures

Neuronal cultures were prepared as described previously [50]. P0–P1 mouse cerebral cortices were dissected and dissociated in 0.25% trypsin (PAA) in DMEM/F12 (Gibco, Invitrogen) for 15 min at 37°C. Trypsin was inactivated by adding an equal volume of DMEM/F12 containing 20% FBS (Lonza, Bio Whittaker). Cerebral cortex was dissociated by trituration in DMEM/F12 containing 10% FBS and 20 µg ml^{-1} DNase I (Roche) using a fire-polished Pasteur pipette. Dissociated cortical neurons were cultured in Neurobasal medium (Gibco, Invitrogen) on 100 µg ml^{-1} poly-L-lysine-coated (Sigma–Aldrich) acid-washed coverslips in a humidified atmosphere with 5% CO_2 at 37°C.

4.6. Neuronal transfection and analysis

Neurons were transfected as described previously [50]. Briefly, at DIV2, neurons in culture were transfected by Lipofectamine LTX according to the manufacturer's protocol (Invitrogen), with a full-length Cntn4 construct or an empty pcDNA3.1 control vector. At DIV5, neurons were fixed with 4% PFA and 4% sucrose in PBS, pH 7.4. Immunocytochemistry was performed with the following primary antibodies: rat anti-GFP (Chromotek, 50430-2-AP) 1:500; rabbit anti-Caspase-3 (Cell Signaling Technology, 9664) 1:1000. Images were captured by confocal laser scanning microscopy (Zeiss Axioscop A1). For analysis of neuronal morphological parameters, four independent batch experiments were examined with total analysed cell number n = 279 (Cntn4 OE), n = 439 (EV). WIS-Neuromath software (Weizmann Institute) was used for determining morphological parameters [110], which included soma size, number of branches, total dendrite length and longest dendrite length. For analysis of neuronal apoptosis in the Cntn4 OE experiments, the immunoreactivity of caspase-3 in a mean number of 53 transfected neurons was quantified per condition of each independent experiment (n = 4 for EV and Cntn4 OE, respectively). Positive neurons were analysed by quantification of the number of double-labelled cells as a percentage of the total amount of transfected cells in ImageJ software [109].

4.7. HEK293 cell culture and transfection

HEK293 cells were maintained in high glucose Dulbecco's modified Eagle's medium 5 g l^{-1} glucose (DMEM; Gibco, UK, 11965084). Cell culture media were supplemented with 10% (v/v) heat-inactivated fetal bovine serum (FBS; Gibco, UK, 11550356), 2 mM L-glutamine (PAA) and 1× penicillin/streptomycin (pen/strep; PAA) and cultured in a humidified atmosphere with 5% CO_2 at 37°C. HEK293 cells were transfected using polyethylenimine (PEI; Polysciences) [111] or Lipofectamine LTX (Invitrogen, according to the manufacturer's manual).

4.8. Cell adhesion assay

Cell adhesion assays were performed with HEK293 cells as previously described [50,112]. HEK293 cells were co-transfected either with pEGFP-N1 (Clontech, 6085-1) or pCAG-DsRed-T1 (gift from Prof. Scheiffele) and full-length pcDNA3.1-FLAG-mCntn4, pSFV-huAPP695 [113] (gift from Prof. De Strooper), pCAG-HA-NLGN1 and pCAG-HA-NRXN1β^{-} (last two were gifts from Prof. Scheiffele) expression constructs. Separate populations of HEK293 cells were co-transfected either with Cntn4

together with DsRed or with APP together with EGFP expression plasmids. As a positive control, cells were co-transfected with NLGN1 and DsRed or with NRXN1β⁻ and EGFP expression plasmids. NLGN1 and NRXN1β⁻ are well-established *trans*-binding partners [54,55]. Since Cntn4 can form homodimers in *trans* [56], cells were also co-transfected with Cntn4 and EGFP or Cntn4 with DsRed expression plasmids, as a second positive control. As a negative control, cells were transfected with either DsRed or EGFP expression plasmids. Cells expressing DsRed, NRXN1β⁻ or APP, were incubated with cells expressing EGFP, NLGN1 or Cntn4. As a negative control, cells expressing DsRed were incubated with cells expressing EGFP. After 48 h, the cells were detached using 1 mM EDTA in PBS, pH 7.4 and centrifuged at 1000 r.p.m. for 5 min. The pellets were resuspended in suspension medium (10% HIFCS, 50 mM Hepes-NaOH pH 7.4, 10 mM $CaCl_2$ and 10 mM $MgCl_2$ and combined to a total of 5×10^6 (1:1) in 0.3 ml total volume of 0.5 ml Eppendorf tubes. The cell mixtures were incubated at RT under gentle agitation. The extent of cell aggregation was assessed at 90 min by removing aliquots, spotting them onto culture slides and imaging by a Leica AF6000 microscope (Leica, UK). The resulting images were then analysed by counting the number and size of particles using ImageJ. An arbitrary value for particle size was then set as a threshold based on negative control values. The aggregation index was calculated by expressing the number of particles participating in aggregation as a percentage of the total particles in 5–10 fields of 1.509 mm^2 per cell suspension combination of each independent experiment ($n = 3$).

4.9. Cell surface binding assay

To investigate whether CNTN4 interacts with APP, a cell surface binding assay was used with slight modifications [114]. Transfection of HEK293 cells with pIGplus-RGMa-Fc or pSFV-huAPP695 was performed. Forty-eight hours after transfection the medium with soluble RGMA-Fc or APP was concentrated through a 50 000 kDa column (YM-50, Millipore). The concentrated proteins were supplemented with Dulbecco's modified Eagle's medium 1 g l^{-1} glucose (DMEM; Gibco, Invitrogen) with 2 mM L-glutamine (PAA) and 1× penicillin/streptomycin (pen/strep; PAA) and distributed in six-well plates with HEK293 cells transfected with Neo1.a-AP-His (Addgene #71963) or pcDNA3.1-Cntn4-FLAG. Binding between the proteins was allowed overnight in a humidified atmosphere with 5% CO_2 at 37°C. Cells were fixed with 4% PFA in PBS, pH 7.4 and 0.01% sodium azide. Immunocytochemistry was performed with the following primary antibodies: rabbit anti-FLAG (20543-1-AP, Proteintech) 1:200, rabbit anti-His (10001-0-AP, Proteintech) 1:200, goat anti-APP (AF1168, R&D Systems) 200 µg ml^{-1}, mouse anti-Fc (M4280, Sigma Aldrich) 1:100. Appropriate secondary antibodies were used from the Molecular Probes Alexa Series (1:250, Invitrogen). For the cell surface binding analysis, images from the Leica AF6000 microscope (Leica, UK) were used. Analyses were performed of about 300 transfected cells per condition of each independent experiment ($n = 3$). The images were analysed by quantification of the number of double-labelled cells as a percentage of the total amount of transfected cells in ImageJ. Statistical analysis was carried out using unpaired Student's *t* test.

4.10. Immunoprecipitation

IP experiments were performed using GFP-Trap-A beads (Chromotek, gta), according to the manufacturer's manual, as previously described [50]. A biotin- and GFP-tagged extracellular rat *Cntn4* (CNTN4-TMGFPBio) fusion protein was generated by subcloning the coding sequence of the extracellular CNTN4 domains (NM_053879.1: nt 476-3394), excluding the coding sequence of the GPI anchor. This was amplified from wild-type *Cntn4* cDNA (BluescriptIISK-CNTN4) and ligated to the sequence of plexin-A1 transmembrane domain coding sequence (NM_008881.2: nt 3962-4123). The coding sequences of a five glycine linker and intracellular GFP and biotin tags followed and were inserted in a pcDNA3.1(-)/myc-His (Invitrogen) vector backbone. The control vector (TMGFPBio) is identical, but it is truncated beyond the transmembrane domain.

For proteomics, HEK293 cells expressing the indicated GFP-tagged fusion proteins were collected in ice-cold PBS and centrifuged at 1000 r.p.m. in a pre-cooled centrifuge at 4°C for 5 min. Cell pellets were lysed in lysis buffer (10 mM Tris-HCl, pH 7.5, 150 mM NaCl, 0.5 mM EDTA, 0.5% NP40, 1 mM PMSF and complete protease inhibitor cocktail (Roche)), incubated on ice for 30 min and centrifuged at 13 200 r.p.m. at 4°C for 10 min. Cleared supernatant containing roughly 5.4–6.6 mg of protein was mixed with 50 µl GFP-Trap-A agarose beads (Chromotek), which had been equilibrated in dilution buffer (10 mM Tris-HCl, pH 7.5, 150 mM NaCl, 0.5 mM EDTA, 1 mM PMSF and complete protease inhibitor cocktail (Roche)) at 4°C. After 1.5 h incubation at 4°C, beads were washed twice in dilution buffer. Precipitated proteins were eluted by boiling the pull-down samples in NuPAGE LDS sample buffer (Invitrogen) containing 2% β-mercaptoethanol at 95°C for 10 min.

Thirty microlitres of each sample was run on a 12% Bis-Tris 1D SDS-PAGE gel (Biorad) either for 2–3 cm or was run completely and stained with colloidal Coomassie dye G-250 (Gel Code Blue Stain Reagent, Thermo Scientific). The lane was cut into bands, which were treated with 6.5 mM dithiothreitol for 1 h at 60°C for reduction and 54 mM iodoacetamide for 30 min for alkylation. The proteins were digested overnight with trypsin (Promega) at 37°C. The peptides were extracted with acetonitrile and dried in a vacuum concentrator.

4.11. Mass spectrometry: RP-NanoLC-MS/MS

Mass spectrometry data were acquired as previously described [50]. Data were acquired using an LTQ-Orbitrap coupled to an Agilent 1200 system or an Obritrap Q Exactive mass spectrometer connected to an Agilent 1290 system. In the case of the LTQ-Orbitrap, peptides were first trapped ((Dr Maisch GmbH) Reprosil C18, 3 µm, 2 cm × 100 µm) before being separated on an analytical column (50 µm × 400 mm, 3 µm, 120 Å, Reprosil C18-AQ). Trapping was performed at 5 µl min^{-1} for 10 min in solvent A (0.1 M acetic acid in water) and the gradient was as follows: 10–37% solvent B (0.1 M acetic acid in 80% acetonitrile) in 30 min,

37–100% B in 2 min, 100% B for 3 min and finally solvent A for 15 min. The flow was passively split to 100 nl min^{-1}. Data were acquired in a data-dependent manner, to automatically switch between MS and MS/MS. Full scan MS spectra from *m*/*z* 350 to 1500 were acquired in the Orbitrap at a target value of 5e5 with a resolution of 60 000 at *m*/*z* 400 in the case of the LTQ-Orbitrap XL and 30 000 for the LTQ-Discovery. The five most intense ions were selected for fragmentation in the linear ion trap at a normalized collision energy of 35% after the accumulation of a target value of 10 000. In the case of the Q Exactive samples were first trapped ((Dr Maisch GmbH) Reprosil C18, 3 µm, 2 cm × 100 µm) before being separated on an analytical column (Agilent Poroshell EC-C18, 2.7 µm, 40 cm × 50 µm). Trapping was performed for 10 min in solvent A and the gradient was as follows: 13–41% solvent B in 35 min, 41–100% in 3 min and finally solvent A for 10 min. The flow was passively split to 100 nl min^{-1}. The mass spectrometer was operated in data-dependent mode. Full scan MS spectra from *m*/*z* 350 to 1500 were acquired at a resolution of 35 000 at *m*/*z* 400 after accumulation to a target value of 3e6. Up to 10 most intense precursor ions were selected for fragmentation. HCD fragmentation was performed at normalized collision energy of 25% after the accumulation to a target value of 5e4. MS/MS was acquired at a resolution of 17.500. In all cases, nano-electrospray was performed at 1.7 kV using an in-house made gold-coated fused silica capillary (o.d. 360 µm; i.d. 20 µm; tip i.d. 10 µm).

4.12. Proteomics data analysis

Raw files were processed using Proteome Discoverer 1.3 (v. 1.3.0.339, Thermo Scientific Bremen, Germany). The database search was performed against the Swissprot database (v. August 2014) using Mascot (v. 2.4.1, Matrix Science, UK) as search engine. Carbamidomethylation of cysteines was set as a fixed modification and oxidation of methionines was set up as a variable modification. Trypsin was specified as enzyme and up to two miss cleavages were allowed. Data filtering was performed using the percolator, resulting in 1% false-discovery rate. An additional filter was Mascot ion score greater than 20. Raw files corresponding to one sample were merged into one result file. Data were further analysed with Saint [51] using the Crapome web interface in order to identify interacting proteins. Default settings were used for calculating the FC-A and FC-B score. The probability score was calculated using Saint Express performing 20 000 iterations.

4.13. SH-SY5Y cell culture and CRISPR/Cas9 mediated knockout of *CNTN4* and *APP*

Neuroblastoma SH-SY5Y cells were cultured in Dulbecco's modified Eagle's medium with GlutaMAX (DMEM/F-12, Gibco, UK, 10566016) supplemented with 10% (v/v) heat-inactivated foetal bovine serum. CRISPR/Cas9 gene editing was performed as described elsewhere [115]. In brief, sgRNAs were designed in Benchling (Benchling Software, 2020), ordered from Integrated DNA Technologies and cloned into pSpCas9(BB)-2A-GFP(PX458) and pU6-(BbsI)_CBh-Cas9-T2A-mCherry. pSpCas9(BB)-2A-GFP (PX458) was a gift from Feng Zhang (Addgene plasmid #48138; http://n2t.net/addgene:48138; RRID:Addgene_48138). pU6-(BbsI)_CBh-Cas9-T2A-mCherry was a gift from Ralf Kuehn (Addgene plasmid #64324; http://n2t.net/addgene:64324; RRID:Addgene_64324). Paired sgRNAs targeting regions of *CNTN4* and *APP* were designed to generate homozygous knockout in addition to the non-targeting EV control (full sequence detail in electronic supplementary material, table S1). sgRNA plasmids validated by Sanger sequencing were transfected into SH-SY5Y cells using nucleofection (SF Cell Line 4D-Nucelofector X kit, Lonza, Germany, V4XC-2012) according to the manufacturer's protocol. After low-density seeding, single clones were isolated and expanded in 96-well plates. Overall, we sequenced at least 10 clones per construct and confirmed homozygous single-cell clones at least twice by Sanger sequencing. Both indels induced premature stop codons as validated by PCR and Sanger sequencing. *CNTN4* and *APP* deficiencies were further shown at the RNA and protein level using real-time RT-PCR and Western blot, respectively. RNA extraction, cDNA generation and real-time RT-PCR as well as protein extraction and Western blots were performed as previously described [44].

4.14. *In vitro* cell morphology assay

SH-SY5Y cells were differentiated using a continuous application of retinoic acid (RA, Sigma Aldrich, UK) and brain-derived neurotrophic factor (BDNF, Peprotech, UK, 450-02). Differentiation media consisted of DMEM/F-12 (0% FBS), 10 µM RA and 20 ng ml^{-1} BDNF. Cells were differentiated for 5 days, changing the medium every other day. On day 5, cells were fixed with 4% PFA in PBS, pH 7.4. Cells were permeabilized and blocked for 1 h at room temperature. Immunocytochemistry was performed with primary antibody mouse anti-β(III)-Tubulin (R&D Systems, MAB1195) 1:500, with appropriate secondary antibody from the Molecular Probes Alexa Series (1:250, Invitrogen). Nuclei were counter-stained with DAPI. Images were captured by fluorescence microscope (Leica DM4000 LED) with the LAS-X software. For analysis of neuronal morphological parameters, three independent batch experiments were examined with a total analysed cell number of at least $n = 90$ per genotype. Image analysis was carried out in ImageJ, which included cell area, total and longest neurite length.

4.15. Statistical analysis

For statistical analysis, data were plotted as the mean ± s.e.m., unless otherwise stated. Statistical analysis was carried out using ANOVA and unpaired Student's *t* tests where appropriate (Graphpad Prism). Further details are provided in the electronic supplementary material.

Ethics. All experimental procedures were performed according to the institutional guidelines of the University Medical Center (UMC) Utrecht. All animal procedures were performed according to NIH guidelines and approved by the European Council Directive (86/609/EEC).

Data accessibility. Electronic supplementary material is available online [116].

Declaration of AI use. We have not used AI-assisted technologies in creating this article.

Authors' contributions. R.A.B.: data curation, formal analysis, investigation, methodology, project administration, validation, writing—original draft, writing—review and editing; A.Z.: conceptualization, data curation, formal analysis, validation, visualization, writing—review and editing; M.E.: data curation, formal analysis, investigation, methodology, validation; J.J.S.: data curation, formal analysis, validation, visualization; H.P.: data curation, formal analysis, resources, software; R.L.R.E.T.: data curation, formal analysis, resources, software; D.F.: data curation, formal analysis, validation, visualization; A.M.: data curation, investigation, resources; O.J.R.J.: data curation, formal analysis, investigation, methodology, validation; A.K.: data curation, formal analysis, investigation, methodology, validatio; J.G.: data curation, formal analysis, investigation, methodology, validation; U.C.M.: data curation, resources, supervision, Writing—review and editing; M.J.H.K.: conceptualization, funding acquisition, supervision, writing—review and editing; J.P.H.B.:conceptualization, funding acquisition, supervision, writing—review and editing; A.O.-A.: conceptualization, data curation, formal analysis, funding acquisition, investigation, methodology, project administration, resources, software, supervision, validation, visualization, writing—review and editing.

All authors gave final approval for publication and agreed to be held accountable for the work performed therein.

Conflict of interest declaration. We declare we have no competing interests.

Funding. We thank Canon foundation in Europe, ARUKSouth West Network, QUEX Initiator, British Society for Neuroendocrinology, and Northcott Devon Medical Foundation for financial support. U.C.M. and D.F. were supported by grants from Deutsche Forschungsgemeinschaft (MU1457/15-1 and 17-1). M.E. was supported through a QUEX PhD scholarship—a joint initiative of The University of Queensland and the University of Exeter.

Acknowledgements. We thank Dr Yoshihiro Yoshihara, RIKEN BSI, for providing the *Cntn4* mice and helpful advice. We thank Mr Hugo Oppelaar and Mr Henk Spierenburg for performing the genotyping of the animals.

References

1. American Psychiatric Association. 2013 Section II diagnostic criteria and codes. In *Diagnostic and statistical manual of mental disorders* (ed. SE Swedo), pp. 50–59, Arlington, VA: American Psychiatric Publishing. (doi:10.1176/appi.books.9780890425596)
2. Elsabbagh M *et al*. 2012 Global prevalence of autism and other pervasive developmental disorders. *Autism Res.* **5**, 160–179. (doi:10.1002/aur.239)
3. Lord C *et al*. 2012 A multisite study of the clinical diagnosis of different autism spectrum disorders. *Arch. Gen. Psychiatry* **69**, 306–313. (doi:10.1001/archgenpsychiatry.2011.148)
4. Simons Foundation. 2003 SFARI. See https://sfari.org/ (accessed 26 July 2017)
5. Ung DC *et al*. 2018 Ptchd1 deficiency induces excitatory synaptic and cognitive dysfunctions in mouse. *Mol. Psychiatry* **23**, 1356–1367. (doi:10.1038/mp.2017.39)
6. Gandawijaya J, Bamford RA, Burbach JPH, Oguro-Ando A. 2020 Cell adhesion molecules involved in neurodevelopmental pathways implicated in 3p-deletion syndrome and autism spectrum disorder. *Front. Cell. Neurosci.* **14**, 611379. (doi:10.3389/fncel.2020.611379)
7. Culotta L, Penzes P. 2020 Exploring the mechanisms underlying excitation/inhibition imbalance in human iPSC-derived models of ASD. *Mol. Autism* **11**, 32. (doi:10.1186/s13229-020-00339-0)
8. Sohal VS, Rubenstein JLR. 2019 Excitation-inhibition balance as a framework for investigating mechanisms in neuropsychiatric disorders. *Mol. Psychiatry* **24**, 1248–1257. (doi:10.1038/s41380-019-0426-0)
9. Joo Y, Benavides DR. 2021 Local protein translation and RNA processing of synaptic proteins in autism spectrum disorder. *Int. J. Mol. Sci.* **22**, 2811. (doi:10.3390/ijms22062811)
10. Südhof TC. 2021 The cell biology of synapse formation. *J. Cell Biol.* **220**, e202103052. (doi:10.1083/jcb.202103052)
11. Südhof TC. 2018 Towards an understanding of synapse formation. *Neuron* **100**, 276–293. (doi:10.1016/j.neuron.2018.09.040)
12. Südhof TC. 2008 Neuroligins and neurexins link synaptic function to cognitive disease. *Nature* **455**, 903–911. (doi:10.1038/nature07456)
13. Corfas G, Velardez MO, Ko CP, Ratner N, Peles E. 2004 Mechanisms and roles of axon-Schwann cell interactions. *J. Neurosci.* **24**, 9250–9260. (doi:10.1523/JNEUROSCI.3649-04.2004)
14. Ko J, Zhang C, Arac D, Boucard AA, Brunger AT, Südhof TC. 2009 Neuroligin-1 performs neurexin-dependent and neurexin-independent functions in synapse validation. *EMBO J.* **28**, 3244–3255. (doi:10.1038/emboj.2009.249)
15. Zhang C *et al*. 2009 A neuroligin-4 missense mutation associated with autism impairs neuroligin-4 folding and endoplasmic reticulum export. *J. Neurosci.* **29**, 10 843–10 854. (doi:10.1523/JNEUROSCI.1248-09.2009)
16. Alarcón M *et al*. 2008 Linkage, association, and gene-expression analyses identify CNTNAP2 as an autism-susceptibility gene. *Am. J. Hum. Genet.* **82**, 150–159. (doi:10.1016/j.ajhg.2007.09.005)
17. Arking DE *et al*. 2008 A common genetic variant in the neurexin superfamily member CNTNAP2 increases familial risk of autism. *Am. J. Hum. Genet.* **82**, 160–164. (doi:10.1016/j.ajhg.2007.09.015)
18. Bakkaloglu B *et al*. 2008 Molecular cytogenetic analysis and resequencing of contactin associated protein-like 2 in autism spectrum disorders. *Am. J. Hum. Genet.* **82**, 165–173. (doi:10.1016/j.ajhg.2007.09.017)
19. Rossi E *et al*. 2008 A 12Mb deletion at 7q33-q35 associated with autism spectrum disorders and primary amenorrhea. *Eur. J. Med. Genet.* **51**, 631–638. (doi:10.1016/j.ejmg.2008.06.010)
20. Wass S. 2011 Distortions and disconnections: disrupted brain connectivity in autism. *Brain Cogn.* **75**, 18–28. (doi:10.1016/j.bandc.2010.10.005)
21. Sytnyk V, Leshchyns'ka I, Schachner M. 2017 Neural Cell Adhesion Molecules of the Immunoglobulin Superfamily Regulate Synapse Formation, Maintenance, and Function. *Trends Neurosci.* **40**, 295–308. (doi:10.1016/j.tins.2017.03.003)
22. Betancur C, Sakurai T, Buxbaum JD. 2009 The emerging role of synaptic cell-adhesion pathways in the pathogenesis of autism spectrum disorders. *Trends Neurosci.* **32**, 402–412. (doi:10.1016/j.tins.2009.04.003)
23. Bhat S, Acharya UR, Adeli H, Bairy GM, Adeli A. 2014 Autism: cause factors, early diagnosis and therapies. *Rev. Neurosci.* **25**, 841–850. (doi:10.1515/revneuro-2014-0056)
24. Casanova MF. 2007 The neuropathology of autism. *Brain Pathol.* **17**, 422–433. (doi:10.1111/j.1750-3639.2007.00100.x)
25. Levitt P, Eagleson KL, Powell EM. 2004 Regulation of neocortical interneuron development and the implications for neurodevelopmental disorders. *Trends Neurosci.* **27**, 400–406. (doi:10.1016/j.tins.2004.05.008)

26. Ecker C, Bookheimer SY, Murphy DGM. 2015 Neuroimaging in autism spectrum disorder: brain structure and function across the lifespan. *Lancet. Neurol.* **14,**1121–1134, (doi:10.1016/S1474-4422(15)00050-2B1)
27. Shimoda Y, Watanabe K. 2009 Contactins. *Cell Adh. Migr.* **3**, 64–70. (doi:10.4161/cam.3.1.7764)
28. Oguro-Ando A, Zuko A, Kleijer KTE, Burbach JPH. 2017 A current view on contactin-4, -5, and -6: implications in neurodevelopmental disorders. *Mol. Cell. Neurosci.* **81,**72–83, (doi:10.1016/j.mcn.2016.12.004B3)
29. Zuko A, Kleijer KTE, Oguro-Ando A, Kas MJH, van Daalen E, van der Zwaag B, Burbach JPH. 2013 Contactins in the neurobiology of autism. *Eur. J. Pharmacol.* **719,**63–74, (doi:10.1016/j.ejphar.2013.07.016B3)
30. Chatterjee M, Schild D, Teunissen CE. 2019 Contactins in the central nervous system: role in health and disease. *Neural Regen. Res.* **14**, 206–216. (doi:10.4103/1673-5374.244776)
31. Berg JM, Geschwind DH. 2012 Autism genetics: searching for specificity and convergence. *Genome Biol.* **13**, 247. (doi:10.1186/gb4034)
32. Glessner JT *et al*. 2009 Autism genome-wide copy number variation reveals ubiquitin and neuronal genes. *Nature* **459**, 569–573. (doi:10.1038/nature07953)
33. Torres F, Barbosa M, Maciel P. 2016 Recurrent copy number variations as risk factors for neurodevelopmental disorders: critical overview and analysis of clinical implications. *J. Med. Genet.* **53**, 73–90. (doi:10.1136/jmedgenet-2015-103366)
34. Kirov G. 2015 CNVs in neuropsychiatric disorders. *Hum. Mol. Genet.* **24**, R45–R49. (doi:10.1093/hmg/ddv253)
35. Guo H *et al*. 2012 Disruption of contactin 4 in two subjects with autism in Chinese population. *Gene* **505**, 201–205. (doi:10.1016/j.gene.2012.06.051)
36. Fernandez T, Morgan T, Davis N, Klin A, Morris A, Farhi A, Lifton RP, State MW. 2008 Disruption of Contactin 4 (CNTN4) results in developmental delay and other features of 3p deletion syndrome. *Am. J. Hum. Genet.* **82**, 57505. (doi:10.1016/j.ajhg.2008.04.021)
37. Roohi J, Montagna C, Tegay DH, Palmer LE, DeVincent C, Pomeroy JC, Christian SL, Nowak N, Hatchwell E. 2009 Disruption of contactin 4 in three subjects with autism spectrum disorder. *J. Med. Genet.* **46**, 176–182. (doi:10.1136/jmg.2008.057505)
38. Yoshihara Y, Kawasaki M, Tamada A, Nagata S, Kagamiyama H, Mori K. 1995 Overlapping and differential expression of BIG-2, BIG-1, TAG-1, and F3: four members of an axon-associated cell adhesion molecule subgroup of the immunoglobulin superfamily. *J. Neurobiol.* **28**, 51–69. (doi:10.1002/neu.480280106)
39. Hodge RD *et al*. 2019 Conserved cell types with divergent features in human versus mouse cortex. *Nature* **573**, 61–68. (doi:10.1038/s41586-019-1506-7)
40. Fernandez T. 2013 . Cntn4: Contactin 4. In *Encyclopedia of autism spectrum disorders*. New York, NY: Springer New York. (doi:10.1007/978-1-4419-1698-3)
41. Kaneko-Goto T, Yoshihara SI, Miyazaki H, Yoshihara Y. 2008 BIG-2 mediates olfactory axon convergence to target glomeruli. *Neuron* **57**, 834–846. (doi:10.1016/j.neuron.2008.01.023)
42. Osterhout JA, Stafford BK, Nguyen PL, Yoshihara Y, Huberman AD. 2015 Contactin-4 mediates axon-target specificity and functional development of the accessory optic system. *Neuron* **86**, 985–999. (doi:10.1016/j.neuron.2015.04.005)
43. Molenhuis RT, Bruining H, Remmelink E, de Visser L, Loos M, Burbach JPH, Kas MJH. 2016 Limited impact of Cntn4 mutation on autism-related traits in developing and adult C57BL/6J mice. *J. Neurodev. Disord.* **8**, 6. (doi:10.1186/s11689-016-9140-2)
44. Oguro-Ando A *et al*. 2021 Cntn4, a risk gene for neuropsychiatric disorders, modulates hippocampal synaptic plasticity and behavior. *Transl. Psychiatry* **11**, 106. (doi:10.1038/s41398-021-01223-y)
45. Gabriele RMC, Abel E, Fox NC, Wray S, Arber C. 2022 Knockdown of amyloid precursor protein: biological consequences and clinical opportunities. *Front. Neurosci.* **16**, 835645. (doi:10.3389/fnins.2022.835645)
46. Müller UC, Deller T, Korte M. 2017 Not just amyloid: physiological functions of the amyloid precursor protein family. *Nat. Rev. Neurosci.* **18**, 281–298. (doi:10.1038/nrn.2017.29)
47. Weyer SW *et al*. 2014 Comparative analysis of single and combined APP/APLP knockouts reveals reduced spine density in APP-KO mice that is prevented by APPsα expression. *Acta Neuropathol. Commun.* **2**, 36. (doi:10.1186/2051-5960-2-36)
48. Ristanović D, Milosević NT, Stulić V. 2006 Application of modified Sholl analysis to neuronal dendritic arborization of the cat spinal cord. *J. Neurosci. Methods* **158**, 212–218. (doi:10.1016/j.jneumeth.2006.05.030)
49. Geiger T, Wehner A, Schaab C, Cox J, Mann M. 2012 Comparative proteomic analysis of eleven common cell lines reveals ubiquitous but varying expression of most proteins. *Mol. Cell. Proteomics* **11**, M111.014050. (doi:10.1074/mcp.M111.014050)
50. Zuko A, *et al*. 2016 Association of cell adhesion molecules contactin-6 and latrophilin-1 regulates neuronal apoptosis. *Front. Mol. Neurosci.* **9**, 1–16. (doi:10.3389/fnmol.2016.00143)
51. Choi H *et al*. 2011 SAINT: probabilistic scoring of affinity purification–mass spectrometry data. *Nat. Methods* **8**, 70–73. (doi:10.1038/nmeth.1541)
52. UniProt Consortium. 2015 UniProt: a hub for protein information. *Nucleic Acids Res.* **43**, D204–D212.
53. Osterfield M, Egelund R, Young LM, Flanagan JG. 2008 Interaction of amyloid precursor protein with contactins and NgCAM in the retinotectal system. *Development* **135**, 1189–1199. (doi:10.1242/dev.007401)
54. Boucard AA, Chubykin AA, Comoletti D, Taylor P, Südhof TC. 2005 A splice code for *trans*-synaptic cell adhesion mediated by binding of neuroligin 1 to α- and β-neurexins. *Neuron* **48**, 229–236. (doi:10.1016/j.neuron.2005.08.026)
55. Nguyen T, Südhof TC. 1997 Binding properties of neuroligin 1 and neurexin 1β reveal function as heterophilic cell adhesion molecules. *J. Biol. Chem.* **272**, 26032–26039. (doi:10.1074/jbc.272.41.26032)
56. Yamagata M, Sanes JR. 2012 Expanding the Ig superfamily code for laminar specificity in retina: expression and role of contactins. *J. Neurosci.* **32**, 14402–14414. (doi:10.1523/JNEUROSCI.3193-12.2012)
57. Paxinos G, Franklin KBJ. 2001 *The mouse brain in stereotaxic coordinates*. San Diego, CA: Elsevier Inc.
58. Chiocchetti AG *et al*. 2016 Transcriptomic signatures of neuronal differentiation and their association with risk genes for autism spectrum and related neuropsychiatric disorders. *Transl. Psychiatry* **6**, e864. (doi:10.1038/tp.2016.119)
59. Haslinger D *et al*. 2018 Loss of the Chr16p11.2 ASD candidate gene QPRT leads to aberrant neuronal differentiation in the SH-SY5Y neuronal cell model. *Mol. Autism* **9**, 1–17. (doi:10.1186/s13229-018-0239-z)
60. Shipley MM, Mangold CA, Szpara ML. 2016 Differentiation of the SH-SY5Y human neuroblastoma cell line. *J. Vis. Exp.* **108**, e53193. (doi:10.3791/53193)
61. Hick M *et al*. 2015 Acute function of secreted amyloid precursor protein fragment APPsα in synaptic plasticity. *Acta Neuropathol.* **129**, 21–37. (doi:10.1007/s00401-014-1368-x)
62. Kaneko-Goto T, Yoshihara SI, Miyazaki H, Yoshihara Y. 2008 BIG-2 mediates olfactory axon convergence to target glomeruli. *Neuron* **57**, 834–846. (doi:10.1016/j.neuron.2008.01.023)
63. Gilbert J, Man HY. 2017 Fundamental elements in autism: from neurogenesis and neurite growth to synaptic plasticity. *Front. Cell. Neurosci.* **11**, 1–25. (doi:10.3389/fncel.2017.00359)

64. Kwan KY, Sestan N, Anton ES. 2012 Transcriptional co-regulation of neuronal migration and laminar identity in the neocortex. *Development* **139**, 1535–1546. (doi:10.1242/dev.069963)
65. Mercati O et al. 2013 Contactin 4, -5 and -6 differentially regulate neuritogenesis while they display identical PTPRG binding sites. *Biol. Open* **2**, 324–334. (doi:10.1242/bio.20133343)
66. Bakos J, Bacova Z, Grant SG, Castejon AM, Ostatnikova D. 2015 Are molecules involved in neuritogenesis and axon guidance related to autism pathogenesis? *Neuromol. Med.* **17**, 297–304. (doi:10.1007/s12017-015-8357-7)
67. Peñagarikano O *et al*. 2011 Absence of CNTNAP2 leads to epilepsy, neuronal migration abnormalities, and core autism-related deficits. *Cell* **147**, 235–246. (doi:10.1016/j.cell.2011.08.040)
68. Kennedy MB. 2000 Signal-processing machines at the postsynaptic density. *Science* **290**, 750–754. (doi:10.1126/science.290.5492.750)
69. Nimchinsky EA, Sabatini BL, Svoboda K. 2002 Structure and function of dendritic spines. *Annu. Rev. Physiol.* **64**, 313–353. (doi:10.1146/annurev.physiol.64.081501.160008)
70. Zhao R et al. 2021 The autism risk gene CNTN4 modulates dendritic spine formation. *Hum. Mol. Genet.* **31**, 207–218. (doi:10.1093/hmg/ddab233)
71. Matus A. 2000 Actin-based plasticity in dendritic spines. *Science* **290**, 754–758. (doi:10.1126/science.290.5492.754)
72. Bamford RA, Widagdo J, Takamura N, Eve M, Anggono V, Oguro-Ando A. 2020 The Interaction between contactin and amyloid precursor protein and its role in Alzheimer's disease. *Neuroscience* **424**184–202, (doi:10.1016/j.neuroscience.2019.10.006)
73. Soba P et al. 2005 Homo- and heterodimerization of APP family members promotes intercellular adhesion. *EMBO J.* **24**, 3624–3634. (doi:10.1038/sj.emboj.7600824)
74. Stahl R, Schilling S, Soba P, Rupp C, Hartmann T, Wagner K, Merdes G, Eggert S, Kins S. 2014 Shedding of APP limits its synaptogenic activity and cell adhesion properties. *Front. Cell. Neurosci.* **8**, 410. (doi:10.3389/fncel.2014.00410)
75. Klevanski M, Saar M, Baumkötter F, Weyer SW, Kins S, Müller UC. 2014 Differential role of APP and APLPs for neuromuscular synaptic morphology and function. *Mol. Cell. Neurosci.* **61**, 201–210. (doi:10.1016/j.mcn.2014.06.004)
76. Ma QH *et al*. 2008 A TAG1-APP signalling pathway through Fe65 negatively modulates neurogenesis. *Nat. Cell Biol.* **10**, 283–294. (doi:10.1038/ncb1690)
77. Steubler V *et al*. 2021 Loss of all three APP family members during development impairs synaptic function and plasticity, disrupts learning, and causes an autism-like phenotype. *EMBO J.* **40**, e107471. (doi:10.15252/embj.2020107471)
78. Nicolas M, Hassan BA. 2014 Amyloid precursor protein and neural development. *Development* **141**, 2543–2548. (doi:10.1242/dev.108712)
79. van der Kant R, Goldstein LSB. 2015 Cellular functions of the amyloid precursor protein from development to dementia. *Dev. Cell* **32**, 502–515. (doi:10.1016/j.devcel.2015.01.022)
80. Young-Pearse TL, Bai J, Chang R, Zheng JB, LoTurco JJ, Selkoe DJ. 2007 A critical function for beta-amyloid precursor protein in neuronal migration revealed by in utero RNA interference. *J. Neurosci.* **27**, 14459–14469. (doi:10.1523/JNEUROSCI.4701-07.2007)
81. Tyan SH *et al*. 2012 Amyloid precursor protein (APP) regulates synaptic structure and function. *Mol. Cell. Neurosci.* **51**, 43–52. (doi:10.1016/j.mcn.2012.07.009)
82. Kögel D, Schomburg R, Copanaki E, Prehn JHM. 2005 Regulation of gene expression by the amyloid precursor protein: inhibition of the JNK/c-Jun pathway. *Cell Death Differ.* **12**, 1–9. (doi:10.1038/sj.cdd.4401495)
83. Mills J, Reiner PB. 1999 Regulation of amyloid precursor protein cleavage. *J. Neurochem.* **72**, 443–460. (doi:10.1046/j.1471-4159.1999.0720443.x)
84. Wu Y, Zhang S, Xu Q, Zou H, Zhou W, Cai F, Li T, Song W. 2016 Regulation of global gene expression and cell proliferation by APP. *Sci. Rep.* **6**, 22460. (doi:10.1038/srep22460)
85. Bouyain S, Watkins DJ. 2010 The protein tyrosine phosphatases PTPRZ and PTPRG bind to distinct members of the contactin family of neural recognition molecules. *Proc. Natl Acad. Sci. USA* **107**, 2443–2448. (doi:10.1073/pnas.0911235107)
86. Nikolaienko RM et al. 2016 Structural basis for interactions between contactin family members and protein-tyrosine phosphatase receptor type G in neural tissues. *J. Biol. Chem.* **291**, 21335–21349. (doi:10.1074/jbc.M116.742163)
87. Ho A, Südhof TC. 2004 Binding of F-spondin to amyloid-beta precursor protein: a candidate amyloid-beta precursor protein ligand that modulates amyloid-beta precursor protein cleavage. *Proc. Natl Acad. Sci. USA* **101**, 2548–2553. (doi:10.1073/pnas.0308655100)
88. Chen CD, Oh SY, Hinman JD, Abraham CR. 2006 Visualization of APP dimerization and APP-Notch2 heterodimerization in living cells using bimolecular fluorescence complementation. *J. Neurochem.* **97**, 30–43. (doi:10.1111/j.1471-4159.2006.03705.x)
89. Cvetkovska V, Ge Y, Xu Q, Li S, Zhang P, Craig AM. 2022 Neurexin-β mediates the synaptogenic activity of amyloid precursor protein. *J. Neurosci.* **42**, 8936–8947. (doi:10.1523/JNEUROSCI.0511-21.2022)
90. Karuppan SJ, Vogt A, Fischer Z, Ladutska A, Swiastyn J, McGraw HF, Bouyain S. 2022 Members of the vertebrate contactin and amyloid precursor protein families interact through a conserved interface. *J. Biol. Chem.* **298**, 101541. (doi:10.1016/j.jbc.2021.101541)
91. Lazarov O, Demars MP. 2012 All in the family: how the APPs regulate neurogenesis. *Front. Neurosci.* **6**, 81. (doi:10.3389/fnins.2012.00081)
92. Dawkins E, Small DH. 2014 Insights into the physiological function of the β-amyloid precursor protein: beyond Alzheimer's disease. *J. Neurochem.* **129**, 756–769. (doi:10.1111/jnc.12675)
93. Mockett BG, Richter M, Abraham WC, Müller UC. 2017 Therapeutic potential of secreted amyloid precursor protein APPsα. *Front. Mol. Neurosci.* **10**, 30. (doi:10.3389/fnmol.2017.00030)
94. Truong PH, Ciccotosto GD, Cappai R. 2019 Analysis of motor function in amyloid precursor-like protein 2 knockout mice: the effects of ageing and sex. *Neurochem. Res.* **44**, 1356–1366. (doi:10.1007/s11064-018-2669-6)
95. Herms J, Anliker B, Heber S, Ring S, Fuhrmann M, Kretzschmar H, Sisodia S, Müller U. 2004 Cortical dysplasia resembling human type 2 lissencephaly in mice lacking all three APP family members. *EMBO J.* **23**, 4106–4115. (doi:10.1038/sj.emboj.7600390)
96. De Jonghe C. 2001 Pathogenic APP mutations near the γ-secretase cleavage site differentially affect Aβ secretion and APP C-terminal fragment stability. *Hum. Mol. Genet.* **10**, 1665–1671. (doi:10.1093/hmg/10.16.1665)
97. Brimberg L, Mader S, Jeganathan V, Berlin R, Coleman TR, Gregersen PK, Huerta PT, Volpe BT, Diamond B. 2016 Caspr2-reactive antibody cloned from a mother of an ASD child mediates an ASD-like phenotype in mice. *Mol. Psychiatry* **21**, 1663–1671. (doi:10.1038/mp.2016.165)
98. Bruining H et al. 2015 Genetic mapping in mice reveals the involvement of pcdh9 in long-term social and object recognition and sensorimotor development. *Biol. Psychiatry* **78**485–495, (doi:10.1016/j.biopsych.2015.01.017)
99. Baranek GT. 1999 Autism during infancy: a retrospective video analysis of sensory-motor and social behaviors at 9–12 months of age. *J. Autism Dev. Disord.* **29**, 213–224. (doi:10.1023/a:1023080005650)
100. Landa R, Garrett-Mayer E. 2006 Development in infants with autism spectrum disorders: a prospective study. *J. Child Psychol. Psychiatry.* **47**, 629–638. (doi:10.1111/j.1469-7610.2006.01531.x)

101. Brian J, Bryson SE, Garon N, Roberts W, Smith IM, Szatmari P, Zwaigenbaum L. 2008 Clinical assessment of autism in high-risk 18-month-olds. *Autism* **12**, 433–456. (doi:10.1177/1362361308094500)
102. Jansiewicz EM, Goldberg MC, Newschaffer CJ, Denckla MB, Landa R, Mostofsky SH. 2006 Motor signs distinguish children with high functioning autism and Asperger's syndrome from controls. *J. Autism Dev. Disord.* **36**, 613–621. (doi:10.1007/s10803-006-0109-y)
103. Freitag CM, Kleser C, Schneider M, von Gontard A. 2007 Quantitative assessment of neuromotor function in adolescents with high functioning autism and Asperger syndrome. *J. Autism Dev. Disord.* **37**, 948–959. (doi:10.1007/s10803-006-0235-6)
104. Nebel MB, Joel SE, Muschelli J, Barber AD, Caffo BS, Pekar JJ, Mostofsky SH. 2014 Disruption of functional organization within the primary motor cortex in children with autism. *Hum. Brain Mapp.* **35**, 567–580. (doi:10.1002/hbm.22188)
105. Nebel MB, Eloyan A, Barber AD, Mostofsky SH. 2014 Precentral gyrus functional connectivity signatures of autism. *Front. Syst. Neurosci.* **8**, 80. (doi:10.3389/fnsys.2014.00080)
106. Mahajan R, Dirlikov B, Crocetti D, Mostofsky SH. 2016 Motor circuit anatomy in children with Autism spectrum disorder with or without attention deficit hyperactivity disorder. *Autism Res.* **9**, 67–81. (doi:10.1002/aur.1497)
107. Mostofsky SH, Burgess MP, Gidley Larson JC. 2007 Increased motor cortex white matter volume predicts motor impairment in autism. *Brain* **130**, 2117–2122. (doi:10.1093/brain/awm129)
108. Li ZW, Stark G, Götz J, Rülicke T, Gschwind M, Huber G, Müller U, Weissmann C. 1996 Generation of mice with a 200-kb amyloid precursor protein gene deletion by Cre recombinase-mediated site-specific recombination in embryonic stem cells. *Proc. Natl. Acad. Sci. USA* **93**, 6158–6162. (doi:10.1073/pnas.93.12.6158)
109. Schneider CA, Rasband WS, Eliceiri KW. 2012 NIH image to imageJ: 25 years of image analysis. *Nat. Methods* **9**, 671–675. (doi:10.1038/nmeth.2089)
110. Rishal I *et al*. 2013 WIS-NeuroMath enables versatile high throughput analyses of neuronal processes. *Dev. Neurobiol.* **73**, 247–256. (doi:10.1002/dneu.22061)
111. Reed SE, Staley EM, Mayginnes JP, Pintel DJ, Tullis GE. 2006 Transfection of mammalian cells using linear polyethylenimine is a simple and effective means of producing recombinant adeno-associated virus vectors. *J. Virol. Methods* **138**, 85–98. (doi:10.1016/j.jviromet.2006.07.024)
112. Ko J, Fuccillo MV, Malenka RC, Südhof TC. 2009 LRRTM2 functions as a neurexin ligand in promoting excitatory synapse formation. *Neuron* **64**, 791–798. (doi:10.1016/j.neuron.2009.12.012)
113. De Strooper B, Simons M, Multhaup G, Van Leuven F, Beyreuther K, Dotti CG. 1995 Production of intracellular amyloid-containing fragments in hippocampal neurons expressing human amyloid precursor protein and protection against amyloidogenesis by subtle amino acid substitutions in the rodent sequence. *EMBO J.* **14**, 4932–4938. (doi:10.1002/j.1460-2075.1995.tb00176.x)
114. Shimoda Y, Koseki F, Itoh M, Toyoshima M, Watanabe K. 2012 A cis-complex of NB-2/contactin-5 with amyloid precursor-like protein 1 is localized on the presynaptic membrane. *Neurosci. Lett.* **510**, 148–153. (doi:10.1016/j.neulet.2012.01.026)
115. Ran FA, Hsu PD, Wright J, Agarwala V, Scott DA, Zhang F. 2013 Genome engineering using the CRISPR-Cas9 system. *Nat. Protoc.* **8**, 2281–2308. (doi:10.1038/nprot.2013.143)
116. Bamford RA, Zuko A, Eve M, Sprengers JJ, Post H, Taggenbrock R. 2024 Supplementary material from CNTN4 modulates neural elongation through Interplay with APP. Figshare. (doi:10.6084/m9.figshare.c.7125279)